Effects of fluid-rock interaction on $^{40}Ar/^{39}Ar$ geochronology in high-pressure rocks (Sesia-Lanzo Zone, Western Alps)

Ralf Halama[1,*], Matthias Konrad-Schmolke[1], Masafumi Sudo[1], Horst R. Marschall[2], Michael Wiedenbeck[3]

[1] Institute of Earth and Environmental Science, University of Potsdam, Karl-Liebknecht-Str. 24-25, 14476 Potsdam, Germany
[2] Woods Hole Oceanographic Institution, 266 Woods Hole Rd., Woods Hole, MA 02543, USA
[3] GFZ German Research Centre for Geosciences, Telegrafenberg, C128, 14473 Potsdam

* Corresponding author contact information:
Ralf Halama
University of Potsdam
Institute of Earth and Environmental Science
Karl-Liebknecht-Str. 24-25
14476 Potsdam
E-mail: rhalama@geo.uni-potsdam.de
Tel: +49-331-977-5783
Fax: +49-331-977-5700

Revised version submitted 01. October 2013

Abstract

In situ UV laser spot $^{40}Ar/^{39}Ar$ analyses of distinct phengite types in eclogite-facies rocks from the Sesia-Lanzo Zone (Western Alps, Italy) were combined with SIMS boron isotope analyses as well as boron (B) and lithium (Li) concentration data to link geochronological information with constraints on fluid-rock interaction. In weakly deformed samples, apparent $^{40}Ar/^{39}Ar$ ages of phengite cores span a range of ~20 Ma, but inverse isochrons define two distinct main high-pressure (HP) phengite core crystallization periods of 88-82 Ma and 77-74 Ma, respectively. The younger cores have on average lower B contents (~36 μg/g) than the older ones (~43-48 μg/g), suggesting that loss of B and resetting of the Ar isotopic system were related. Phengite cores have variable $\delta^{11}B$ values (-18 to -10 ‰), indicating the lack of km scale B homogenization during HP crystallization.

Overprinted phengite rims in the weakly deformed samples generally yield younger apparent $^{40}Ar/^{39}Ar$ ages than the respective cores. They also show variable effects of heterogeneous excess ^{40}Ar incorporation and Ar loss. One acceptable inverse isochron age of 77.1 ±1.1 Ma for rims surrounding older cores (82.6 ±0.6 Ma) overlaps with the second period of core crystallization. Compared to the phengite cores, all rims have lower B and Li abundances but similar $\delta^{11}B$ values (-15 to -9 ‰), reflecting internal redistribution of B and Li and internal fluid buffering of the B isotopic composition during rim growth. The combined observation of younger $^{40}Ar/^{39}Ar$ ages and boron loss, yielding comparable values of both parameters only in cores and rims of different samples, is best explained by a selective metasomatic overprint. In low permeability samples, this overprint caused recrystallization of phengite rims, whereas higher permeability in other samples led to complete recrystallization of phengite grains.

Strongly deformed samples from a several km long, blueschist-facies shear zone contain mylonitic phengite that forms a tightly clustered group of relatively young apparent $^{40}Ar/^{39}Ar$ ages (64.7 to 68.8 Ma), yielding an inverse isochron age of 65.0 ±3.0 Ma. Almost complete B and Li removal in mylonitic phengite is due to leaching into a fluid. The B isotopic composition is significantly heavier than in phengites from the weakly deformed samples, indicating an external control by a high-$\delta^{11}B$ fluid ($\delta^{11}B$ = +7 ±4 ‰). We interpret this result as reflecting phengite recrystallization related to deformation and associated fluid flow in the shear zone. This event also caused partial resetting of the Ar isotope system and further B loss in more permeable rocks of the adjacent unit. We conclude that geochemical

evidence for pervasive or limited fluid flow is crucial for the interpretation of $^{40}Ar/^{39}Ar$ data in partially metasomatized rocks.

Keywords:
$^{40}Ar/^{39}Ar$ geochronology, fluid-rock interaction, boron isotopes, Sesia-Lanzo Zone, metasomatism

1. Introduction

$^{40}Ar/^{39}Ar$ geochronology is one of the most valuable tools for determining the timing of geologic events. For metamorphic rocks, $^{40}Ar/^{39}Ar$ data are commonly used for unraveling metamorphic exhumation and tectonometamorphic timescales (Di Vincenzo et al., 2006; Beltrando et al., 2009; Wiederkehr et al., 2009; Willner et al., 2009; Warren et al., 2012a, b) as well as the timing of fluid-rock interaction processes (Boundy et al., 1997; Di Vincenzo and Palmeri, 2001; Baxter et al., 2002; Warren et al., 2011, 2012c). *In situ* $^{40}Ar/^{39}Ar$ data with high spatial resolution in combination with textural and petrologic information are particularly powerful for obtaining information about P-T conditions, metasomatism and deformation in the history of a rock (Scaillet et al., 1990; Di Vincenzo et al., 2001, 2006; Putlitz et al., 2005; Warren et al., 2011; Willner et al., 2011).

Besides accumulation of radiogenic ^{40}Ar, concentration and isotopic composition of Ar in minerals are modified by recrystallization and thermal diffusion. In general, recrystallization is the dominant mechanism for alteration of the Ar isotopic composition at lower temperatures, whereas diffusion becomes more important at higher temperatures. However, thermally induced Ar loss by diffusion through the crystal lattice is relatively ineffective in comparison with deformation and chemical reaction mechanisms (Hames and Cheney, 1997). Reactive chemical exchanges together with fluid-mediated element transport are, therefore, the main factors controlling the rate of Ar transport and distribution in a rock (Villa, 1998; Di Vincenzo et al., 2006). Intracrystalline Ar diffusion in metamorphic white mica is particularly inefficient at low temperatures and/or high pressures, and little diffusive Ar loss is expected during exhumation from such regions (Warren et al., 2012a). Hence, $^{40}Ar/^{39}Ar$ ages from phengite in eclogite-facies rocks do not necessarily record temperature histories, but rather reflect variations in radiogenic ^{40}Ar acquired during phengite formation and modified by deformation-enhanced recrystallization (Putlitz et al., 2005; Warren et al., 2012b).

In several high pressure (HP) and ultra-high pressure (UHP) rocks, apparent $^{40}Ar/^{39}Ar$ ages that are higher than the expected ages by several tens of million years, but without geological meaning were attributed to the presence of excess ^{40}Ar (Arnaud and Kelley, 1995; Sherlock and Arnaud, 1999; Giorgis et al., 2000; Baxter et al., 2002; Sherlock and Kelley, 2002). The presence of excess ^{40}Ar and apparent older ages in HP/UHP rocks are thought to reflect a closed, fluid-poor system in which radiogenic Ar that was produced from detrital K-bearing phases is not removed (Kelley, 2002; Sherlock and Kelley, 2002). This implies that open system conditions with a zero grain boundary Ar concentration (i.e. no accumulation of radiogenic Ar while the mineral can still exchange Ar with the intergranular fluid) cannot always be assumed in metamorphic systems (Baxter et al., 2002; Warren et al., 2012b, c). Extraneous Ar in (U)HP rocks may be derived from protoliths whose isotopic signature can survive (U)HP metamorphism and exhumation if the system is closed isotopically. In subduction-metamorphosed rocks, other stable and radiogenic isotopic systems, such as O, Sr and Nd, can preserve pre-subduction signatures without significant isotopic exchange during subduction and exhumation, especially under fluid-restricted conditions (Putlitz et al., 2000, 2005; Früh-Green et al., 2001; Halama et al., 2011). Thus it is clear that information about the extent of fluid-rock interaction and its effect on the isotopic composition of Ar is crucial for a correct interpretation of age constraints derived from $^{40}Ar/^{39}Ar$ data.

Boron (B) is a particularly useful element for detecting and quantifying the extent of fluid-rock interaction during metamorphism because B is a relatively mobile element in hydrous fluids (Brenan et al., 1998; Marschall et al., 2007) and a large isotopic fractionation of the two stable B isotopes (^{10}B and ^{11}B) between minerals and fluids has been observed at low temperatures (Wunder et al., 2005). The combined decrease in $\delta^{11}B$ values and B concentrations in across-arc profiles of arc lavas is thought to reflect the effects of B isotope fractionation during progressive dehydration with increasing depth of the Wadati-Benioff zone: The residual rock becomes isotopically lighter due to the preference of the heavy ^{11}B isotope for the fluid and the slab-fluid flux toward the back arc steadily decreases (Ishikawa and Nakamura, 1994; Bebout et al., 1999; Rosner et al., 2003; Marschall et al., 2007). Secondary ion mass spectrometry (SIMS) analyses confirm that slab dehydration significantly lowers $\delta^{11}B$ of subducted oceanic crust and sediments (Peacock and Hervig, 1999; Pabst et al., 2012), but there is a lack of systematic relationships with peak metamorphic conditions pointing to effects of metasomatic overprinting. Boron concentration zoning in metasomatically overprinted micas and amphiboles (Konrad-Schmolke et al., 2011b) and B isotopic zoning in tourmaline that retains information about the metamorphic fluid evolution through the metamorphic history (Bebout and Nakamura, 2003; Marschall et al., 2009) provide evidence for the sensitivity of the B system for fluid-rock interaction processes.

In this study, we investigate how deformation and associated fluid flux affect apparent $^{40}Ar/^{39}Ar$ ages in a profile from a major intracrustal, blueschist-facies shear zone into adjacent eclogite-facies rocks. We have selected samples from the Sesia-Lanzo Zone (Western Alps, Italy) because these samples are well studied in their structural and textural context and they show various stages of metasomatic overprinting in major and trace element mineral chemistry related to deformation in the shear zone (Babist et al., 2006; Konrad-Schmolke et al., 2011a, b). By combining elemental (B, Li) and isotopic ($\delta^{11}B$) tracers of fluid flow with *in situ* $^{40}Ar/^{39}Ar$ dates, we aim to understand the influence of HP metasomatic processes on $^{40}Ar/^{39}Ar$ geochronology and to test whether deformation and fluid-rock interaction are the principal mechanisms for radiogenic ^{40}Ar loss from white micas (Hames & Cheney, 1997). Moreover, a large geochronological database obtained from a plethora of methods provides a valuable framework for testing the $^{40}Ar/^{39}Ar$ age information (e.g., Oberhänsli et al., 1985; Inger et al., 1996; Reddy et al., 1996; Duchêne et al., 1997; Ruffet et al., 1997; Rubatto et al., 2011).

2. Geologic Setting

The Western Alpine Sesia-Lanzo Zone (SLZ) is a section of polymetamorphic Austroalpine continental crust of the African-Adriatic plate that has reached eclogite-facies conditions during Alpine metamorphism. The following summary of its geologic history is based on the review by Beltrando et al. (2010) and references therein.

Since the Cretaceous, the Western Alps formed due to convergence between Europe and Adria, the latter considered as promontory of Africa or an independent micro-plate. The continental basement units of the SLZ originated from the Adriatic margin and form today the structurally uppermost part of an axial belt comprising continental units derived from Adriatic and European margins and oceanic units form the Mesozoic Piemonte-Liguria Ocean (Fig. 1a). To the East, the SLZ is bounded by the Insubric Line and the Southern Alps, whereas sub-continental peridotites of the Lanzo Massif border the SLZ to the South. Continental units from the European margin and oceanic units from the Tethys Ocean, together part of the Penninic Domain, occur to the West of the SLZ. The subducted oceanic rocks were exhumed in the footwall of the SLZ during convergence prior to continent-continent collision (Babist et al., 2006).

The SLZ is subdivided into three distinct subunits based on lithology and metamorphic grade (Fig. 1a), although slightly different subdivisions have also been proposed (Venturini et al., 1994; Babist et al., 2006). The easternmost of the three SW-NE trending units is the Eclogitic Micaschist Complex (EMS), which is a polymetamorphic basement that includes paragneisses, minor metabasic rocks and marbles. Granitoids and minor gabbros intruded this basement during Carboniferous and Permian times. The EMS reached eclogite-facies conditions of 1.5-2.0 GPa and 550-600 °C during Alpine metamorphism, but is internally only weakly deformed (Konrad-Schmolke et al., 2006). The eclogitic assemblages overprint relict Permian amphibolite-granulite assemblages in the EMS. The Gneiss Minuti (GM) comprise orthogneisses derived from Permian granitoids that intruded into Variscan basement and metamorphosed rocks from a Mesozoic sedimentary sequence, mainly meta-arkose with minor marble, calcschist and metachert. Alpine peak metamorphic conditions in the GM reached 1.0-1.5 GPa at 500-550 °C, but they have experienced a pervasive greenschist-facies metamorphic overprint. Along the contact between EMS and GM, the Seconda Zona Diorito-Kinzigitica (IIDK) crops out discontinuously (Fig. 1a). The IIDK represents pre-Alpine slice of lower crustal, amphibolite-facies micaschists with subordinate amounts of mafic granulites, amphibolites and marbles. Re-equilibration during Alpine metamorphism occurred under blueschist-facies conditions, but is restricted to the margins of the discrete slivers or to narrow shear zones.

One major shear zone separating the EMS from the GM is the Tallorno Shear Zone (TSZ) with a length of approximately 20 km and a width of 1-2 km (Fig. 1b; Konrad-Schmolke et al., 2011a). Deformation in the TSZ was active under blueschist-facies conditions, forming garnet-bearing plagioclase–epidote–sodic amphibole–paragonite–phengite mylonites (Babist et al., 2006). During juxtaposition of the two major lithologic units, contemporaneous subduction of oceanic crust from the Piemonte-Liguria Ocean provided supply of dehydration fluids. A strain- and recrystallization gradient in the EMS was induced by the displacements along and fluid flow within the TSZ. Samples were taken along a ~5 km long profile from the TSZ into the EMS in the Chiusella Valley, which cuts in NW-SE direction through the SLZ (Fig. 1b). Sample MK-99 was taken about 16 km to the NE of sample TSZR in the Nantay Valley, a tributary to the Lys Valley, and is projected onto the cross-section.

3. Petrography and Mineral Chemistry

The samples can be subdivided into weakly deformed, fine- to medium-grained rocks from the EMS unit (samples MK-30, MK-52, MK-55 and 3i) and fine-grained mylonites from the Tallorno Shear Zone (samples TSZR and MK-99). All samples, except sample 3i, were previously described and investigated for major and trace element abundances in the main mineral phases by Konrad-Schmolke et al. (2011a, b), and the following summary is based on this work.

The EMS samples are moderately foliated and comprise two felsic gneisses (MK-30 and MK-55), a mafic gneiss (MK-52) and a micaschist (3i). All EMS samples have a preserved HP mineral assemblage of quartz + phengite + omphacite (or pseudomorphs after omphacite) + sodic amphibole + garnet + rutile + paragonite. The felsic samples are rich in quartz and phengite. The micaschist (3i) contains large phengite flakes up to 0.5 cm in size. The mafic gneiss (MK-52) shows compositional banding and is dominated by sodic amphibole, garnet and omphacite. The foliation is parallel to the compositional banding and interpreted to be syn-kinematic with respect to the mylonitic blueschist-facies shear zone at the EMS-GM contact (Babist et al., 2006). Two stages of retrograde overprint in the stability field of sodic amphibole and a third, weakly developed greenschist-facies overprint were identified in the EMS samples. Both phengite and sodic amphibole show major element compositional differences between pristine cores and overprinted areas (Fig. 2a). Primary phengite cores have 3.3-3.5 Si per formula unit (p.f.u.) and X_{Mg} between 0.70 and 0.85 (Fig. 2b). Chemical modifications occur at the grain boundaries and around inclusions and include a decrease in X_{Mg} to values around 0.6-0.7 (Fig. 2b), lower Na and Sr and higher Ba and Cl contents. Overprinting of phengite is occasionally associated with an increase in Si contents (Fig. 2c). Thermodynamic modeling (Konrad-Schmolke et al., 2011a) demonstrates that a significant amount of water (1.0-1.5 wt.%) must have been present on the retrograde path to maintain water saturation and to produce the newly formed rim compositions and retrograde mineral assemblages. The step-like compositional zoning contradicts a continuous thermodynamic equilibration during exhumation. Instead, it demonstrates the effects of discrete fluid-rock interaction stages during decompression and an associated modification of the major element chemistry of phengite and sodic amphibole (Konrad-Schmolke et al., 2011a, b). Overprinting in the weakly deformed EMS samples collected at some distance to the Tallorno Shear Zone is restricted to narrow, clearly separated zones along grain boundaries and fluid pathways. The rapid water re-saturation and the partial compositional equilibration of the mineral assemblage due to pervasive fluid influx along grain boundaries must have occurred under blueschist-facies conditions, since the observed phengite and amphibole rim compositions are calculated to be stable between 1.1 and 1.4 GPa (Fig. 2d).

The mylonitic samples from the Tallorno Shear Zone comprise a felsic (TSZR) and a mafic (MK-99), fine-grained schist. Major mineral phases are garnet + epidote + albite + phengite + sodic amphibole ± chlorite. Omphacite is lacking, but there are scarce relicts of garnet and/or cores of sodic amphibole. Neither of the two mylonites shows petrographically or chemically distinct phengite rims, but relict flakes of pre-kinematic phengite occur in sample TSZR. A greenschist-facies overprint is evident from chlorite replacing garnet and chlorite + albite replacing sodic amphibole. The mylonitic rocks are well equilibrated under retrograde blueschist-facies conditions, and the minerals are compositionally more homogeneous than in the weakly deformed EMS unit. Phengite in the mylonites is typically fine-grained (5-200 μm), chemically homogenous with Si contents of 3.3 and 3.5 p.f.u. in felsic and mafic samples, respectively. The weakly zoned, mm-sized phengite clasts show decreasing trends in X_{Mg} from core (0.8) to rim (0.6). The small, mylonitic phengite has a major element composition and X_{Mg} similar to the rims of the large grains.

Boron (B) and lithium (Li) concentrations decrease systematically from phengite cores via rims in the weakly deformed samples towards the mylonitic phengites (Fig. 3a; Konrad-Schmolke et al., 2011b). The modifications were explained and successfully modeled by fluid infiltration. Initially, phengite (and amphibole) compositions equilibrated with the infiltrating fluid, so that the composition changed towards the observed rim values. In samples where fluid percolation continued, Li and B were depleted further until eventually, this leaching effect produced the low Li and B contents in the mylonitic samples. The amount of percolating fluid controlled the extent of Li and B depletion, and the retrograde fluid influx evidently increased from the weakly deformed EMS samples towards the highly deformed mylonites. Distinct fluid-rock ratios for crystallization of the overprinted rims (~0.2) and the mylonitic phengites (~4) can explain the distinct Li/B ratios. In summary, fluid-rock interaction with low fluid influx at blueschist-facies conditions led to partial re-hydration and re-equilibration of eclogite-facies mineral assemblages in the EMS, whereas the mylonites from the TSZ experienced high fluid influx and consequently a more pronounced re-equilibration.

Based on the distinct compositions that are related to variable degrees of fluid overprinting, the selected samples are ideally suited to study fluid-rock interaction using B isotopes. Moreover, the elevated Fe contents in phengite rims cause chemical contrasts that can be easily visualized using BSE images, so that areas most suitable for *in situ* $^{40}Ar/^{39}Ar$ analyses can be identified.

4. Analytical methods

4.1. Secondary ion mass spectrometry (SIMS) boron isotope measurements

Boron isotope measurements were completed in Heidelberg and Potsdam, and although similar approaches were used, details of the different procedures are given separately below. Boron isotopic compositions of samples are reported using the δ-notation ($\delta^{11}B$ in ‰) relative to NBS-SRM 951, which has an assigned $^{11}B/^{10}B$ value of 4.043627 (Catanzaro et al., 1970).

4.1.1. Institut für Geowissenschaften, Universität Heidelberg

Boron isotope ratios of phengite were measured with a modified Cameca IMS 3f ion microprobe equipped with a primary beam mass filter. The primary ion beam was $^{16}O^{-}$ accelerated to 10 keV with a beam current of 30 nA, resulting in a beam diameter of ~40 μm and count rates of ~2×10^{4} s^{-1} and ~ 5×10^{3} s^{-1} for ^{11}B and ^{10}B, respectively. The energy window was set to 100 eV without offset. Mass resolution (M/ΔM) was ~1185. Each analysis spot was presputtered for 5 min before 200 cycles were measured with counting times of 3.307 s on ^{10}B and 1.660 s on ^{11}B. The settling time between two different masses was 200 ms, resulting in a total analysis time for one spot of ~25 min. Instrumental mass fractionation was determined by using phengite sample Phe-80-3 (Klemme et al., 2011), which is chemically homogenous and has previously been analyzed by SIMS and TIMS yielding $\delta^{11}B$ values of -14.8 ±2.8 ‰ (1s, n=10) and -13.50 ±0.35 ‰ (1s, n=2), respectively (Pabst et al., 2012). The analytical uncertainty is typically ≤2 ‰ for the weakly deformed samples (~20-60 μg/g B) and <4 ‰ for the low-B (<10 μg/g B) mylonitic samples, as based on the observed distribution of the 200 ratios obtained from a single measurement.

4.1.2. GeoForschungsZentrum, Potsdam

Phengite and paragonite $^{11}B/^{10}B$ ratios on Au-coated thin sections were determined by using a Cameca IMS 6f ion microprobe. Prior to each analysis, a 60 s at 25 nA presputter was applied in order to remove the gold coat and to establish equilibrium sputtering conditions. The mass spectrometer was operated at mass resolving power M/ΔM ~ 1200, sufficient to separate the isobaric interference of $^{10}B^{1}H$ on the ^{11}B mass station and the $^{9}Be^{1}H$ peak on ^{10}B (Trumbull et al., 2009). $^{11}B/^{10}B$ ratios were measured over 250 cycles and counting times per cycle on ^{10}B and ^{11}B were 2 and 4 s, respectively. A 12.5 keV $^{16}O^{-}$ primary beam was focused to about 35 μm diameter on the sample surface. The beam current was set to 25 nA. A 150 μm diameter contrast aperture, a 1800 μm field aperture (equivalent to a field of view 150 μm in diameter) and 50 eV energy window were used without voltage offset.

Instrumental mass fractionation was corrected using NIST SRM 610 glass; as this is not well matched to the matrices studied in this investigation we cannot rule out the presence of some systematic offset in the data reported here (see also Rosner et al. (2008) for a discussion of matrix effects within silicate glasses). The reference material was analyzed at the start and end of each daily section and before changing of samples. The analytical uncertainty is ≤ 2‰ (1s) for samples with moderate B contents and <6‰ for mylonitic samples with very low B contents (< 5 μg/g B), as based on the 250 cycles of data which were collected.

4.2. *In situ* $^{40}Ar/^{39}Ar$ analyses

$^{40}Ar/^{39}Ar$ dating was carried out at the Institute of Earth and Environmental Science, Universität Potsdam, after neutron activation of polished thick sections (1 cm diameter and less than 1 mm thickness) at the Geesthacht Neutron Facility (GeNF) of the GKSS research center in Geesthacht, Germany. Details about sample preparation, neutron activation and Ar isotopic analyses are given in Wiederkehr et al. (2009) and Wilke et al. (2010) and are summarized here. Back-scattered electron images of the sections were obtained to select the most suitable phengite core and rim locations for the *in situ* Ar isotopic analyses. Samples were wrapped in aluminium foil and placed in capsules made of 99.999% Al. The capsules were shielded with 0.5 mm thick Cd foil and irradiated with fast neutrons at a flux rate of 1×10^{12} n cm^{-2} s^{-1} for 97 h. Together with the samples, Fish Canyon Tuff (FCT) sanidine, FC3 sanidine, was irradiated to monitor neutron flux and its spatial variation and to derive J values. The FC3 sanidine was prepared by the Geological Survey of Japan (GSJ) and the age of 27.5 Ma was determined by K-Ar dating of FC3 biotite at GSJ (Uto et al., 1997; Ishizuka, 1998). This age of 27.5 Ma is consistent with the age obtained by the USGS (Lanphere and Baadsgaard, 2001) and both laboratories determined the ages by first principles calibration (Lanphere and Dalrymple, 2000). The true age of the FCT sanidine is in dispute, and alternative ages of 27.93 Ma (Channell et al., 2010), 28.02 Ma (Renne et al. 1998), 28.201 Ma (Kuiper et al., 2008) and 28.305 Ma (Renne et al., 2010) were also reported. Although higher values are apparently more compatible with U-Pb ages, the age used here is based on the value determined by first principles calibrations, which have been independently verified by different laboratories in Japan and the US (Lanphere and Dalrymple, 2000; Lanphere, 2004). Moreover, K_2SO_4 and CaF_2 crystals were irradiated for the correction of Ar isotope interferences produced by reactions of the neutron flux with K or Ca in the samples. SORI93 biotite (92.6 ±0.6 Ma; Sudo et al., 1998) and HD-B1 biotite (24.2 ±0.3 Ma, Hess and Lippolt, 1994; 24.18 ±0.09 Ma, Schwarz and Trieloff, 2007) were irradiated and analyzed to check accuracy and precision of the age determinations.

The Ar isotopic analytical system consists of a New Wave Gantry Dual Wave laser ablation system, an ultrahigh-vacuum purification line, and a Micromass 5400 noble gas mass spectrometer (Wiederkehr et al., 2009; Willner et al., 2011). The laser with a frequency-quadrupled wavelength of 266 nm was operated with a beam size of 50-80 μm, a repetition rate of 10 Hz and a continuous duration of ablation for 2 min to extract gas from the samples. For the weakly deformed EMS samples, this spot size was sufficiently small to analyze single spots or lines in a certain domain (core or rim) of the phengite crystals. Only in the mylonitized samples, where the phengite grain size is smaller, line analyses include domains with several phengite crystals and some matrix material. The extracted gas is purified in the ultra-high vacuum line via SAES getter pumps and a cold trap for 10 min. Two Zr-Al SAES getters are used for the purification of sample gas at 400 °C and room temperature, respectively. The cold trap is kept at -90°C through ethanol cooled by an electric immersion cooler equipped with a stainless steel cooling finger. The high sensitivity, low background sector-type mass spectrometer used for Ar isotopic analysis is equipped with an electron multiplier pulse counting system for analyzing small amounts of Ar. Blanks were run at the start of each session and after every three unknowns. The raw data were corrected for procedural blank contributions, mass discrimination by analysis of atmospheric Ar, and decay of radiogenic ^{37}Ar and ^{39}Ar isotopes produced by irradiation. For blank correction, averages of the blanks measured before and after the unknowns were used. Beam intensities during blank measurements typically were 4.3-6.5 x 10^{-5} V for ^{40}Ar, 4.3-7.5 x 10^{-8} V for ^{39}Ar, 6.6 x 10^{-8} – 1.8 x 10^{-7} V for ^{38}Ar, 3.2-5.7 x 10^{-7} V for ^{37}Ar and 4.6-6.5 x 10^{-7} V for ^{36}Ar. Beam intensity ratios of unknowns to blanks were 5-20 for ^{40}Ar, 380-1130 for ^{39}Ar, 1.7-5.0 for ^{38}Ar, < 0.3 for ^{37}Ar and 0.1-1.5 for ^{36}Ar. For atmospheric and mass discrimination corrections, 295.5 and 0.1869 were used as atmospheric ^{40}Ar/^{36}Ar and ^{38}Ar/^{36}Ar ratios, respectively (Nier et al. 1950). Using a more recently determined alternative atmospheric ratio of 298.56 for ^{40}Ar/^{36}Ar (Lee et al., 2006) would have only minuscule effects on the calculated ^{40}Ar/^{39}Ar dates. Interference corrections of ^{36}Ar produced from ^{40}Ca, ^{39}Ar produced from ^{42}Ca, and ^{40}Ar produced from ^{40}K were also applied. Calculation of ages and errors was performed following Uto et al. (1997) using the total ^{40}K decay constant of 5.543 x 10^{-10} a^{-1} as well as decay constants of 1.978 x 10^{-2} d^{-1} for ^{37}Ar and 2.58 x 10^{-3} a^{-1} for ^{39}Ar. Due to the Cd shielding (0.5 mm Cd) employed, the sample is shielded from thermal neutrons during irradiation. Hence, the levels of $^{38}Ar_{Cl}$, produced via thermal neutron activation of ^{37}Cl, are very low (see

McDougall and Harrison (1999) for discussion) and $^{38}Ar_{Cl}/^{39}Ar_K$ ratios could not be used to trace Cl-rich components. All Ar isotope data are given in the Electronic Annex.

5. Results

5.1. Boron isotopes

Boron isotopic compositions of phengite (Table 1) were analyzed in locations that had been selected based on the BSE images in order to distinguish between cores and rims in the partially overprinted EMS samples. Overall, $\delta^{11}B$ values range from -20 to +6 ‰, and there is a significant difference between the weakly deformed samples with exclusively negative $\delta^{11}B$ (-20 to -6 ‰) and the mylonitic shear zone samples that have a broader range of typically heavier and partly positive $\delta^{11}B$ values (-11 to +6 ‰).

The two felsic gneisses (samples MK-30 and MK-55) have overlapping $\delta^{11}B$ in phengite cores and overprinted rims (Table 1; Fig. 3). However, the overall $\delta^{11}B$ values vary between the two samples: Phengite in gneiss MK-55 ($\delta^{11}B_{cores}$ = -10.0 ±0.9 ‰ [n=3]; $\delta^{11}B_{rims}$ = -9.5 ±1.2 ‰ [n=3]) is isotopically heavier compared to phengite in gneiss MK-30 ($\delta^{11}B_{cores}$ = -14.6 ±0.8 ‰ [n=6]; $\delta^{11}B_{rims}$ = -13.4 ±1.3 ‰ [n=7]). The micaschist (sample 3i) has $\delta^{11}B$ values similar to sample MK-30 with $\delta^{11}B_{cores}$ = -14.3 ±2.2 ‰ [n=6] and $\delta^{11}B_{rims}$ = -15.3 ±2.5 [n=7]. In contrast, the weakly deformed metabasite (sample MK-52) has isotopically lighter phengite cores ($\delta^{11}B_{cores}$ = -17.6 ±3.4 ‰ [n=7]) than rims $\delta^{11}B_{rims}$ = -11.3 ±5.7 ‰ [n=6]), although there is some overlap as well. There is no systematic trend in the three samples relative to the distance to the shear zone. In the mafic mylonite (sample MK-99), $\delta^{11}B$ ranges from -7 to +4 ‰ (average $\delta^{11}B$ = -1.2 ±3.2 ‰ [n=12]). Phengite from the felsic mylonite (sample TSZR) is isotopically most heterogeneous and shows a spread from -11 to +6 ‰ (average $\delta^{11}B$ = -2.3 ±5.3 ‰ [n=9]). The highly negative $\delta^{11}B$ values down to -20.4 ‰ observed in the EMS samples are remarkable, as they are significantly below the typical crustal range (-10 ±3 ‰; Marschall and Jiang, 2011) and >80% of all metamorphic minerals measured in other SIMS studies fall into the range -10 to -2 ‰ (Peacock and Hervig, 1999; Pabst et al., 2012).

5.2. Apparent $^{40}Ar/^{39}Ar$ ages

The apparent $^{40}Ar/^{39}Ar$ ages vary widely and range overall from 57 Ma to 133 Ma with significant variation both within individual samples and among the specific phengite types (cores, rims and mylonitic phengite) (Electronic Annex). Note that there will be a systematic shift towards older ages by 1.5-3% if one of the alternative values for the age of the FCT sanidine standard is used. For the weakly deformed EMS samples, apparent $^{40}Ar/^{39}Ar$ ages of phengite cores cluster in the range 90–70 Ma (Fig. 4). Although there is overlap between core and rim ages, the latter tend to lower values. The most distinct separation of core and rim ages occurs in the micaschist (sample 3i) at ~70 Ma (Fig. 4). Relict cores exhibit a spread of 12 Ma from 82 to 70 Ma with an average of ~75 Ma, whereas overprinted rims yield apparent $^{40}Ar/^{39}Ar$ ages from 57 to 69 Ma, averaging ~62 Ma (Table 2). In the other EMS samples, the apparent $^{40}Ar/^{39}Ar$ ages of phengite cores and rims, respectively, are 92–69 Ma and 88–64 Ma for felsic gneiss MK-30, 88–77 and 86–72 Ma for felsic gneiss MK-55, and 88–82 and 83–79 Ma for mafic gneiss MK-52. In both felsic gneisses, the bulk of the phengite core data falls above ~76 Ma and the respective averages are 84–81 Ma (Table 2), whereas the majority of the overprinted rims ranges in age from 70 to 80 Ma (Fig. 4). The two samples from the TSZ show a larger scatter of apparent $^{40}Ar/^{39}Ar$ ages than the EMS samples (Fig. 5). In the mafic mylonite (sample MK-99), the ages cluster from 90-82 Ma, as ages <80 Ma are completely lacking and three values of ~93 Ma, ~100 Ma and ~111 Ma appear as outliers. The felsic mylonite (sample TSZR) exhibits a tightly clustered group of five apparent $^{40}Ar/^{39}Ar$ ages in the range 68.6–64.7 Ma for mylonitic phengite. The remaining analyses, predominantly obtained in large phengite flakes, yield values from 133 to 79 Ma, the widest range observed in any of the samples.

5.3. Inverse isochrons

Inverse isochron ($^{36}Ar/^{40}Ar$ vs. $^{39}Ar/^{40}Ar$) diagrams were used in conjunction with frequency distribution plots to evaluate the age significance of the $^{40}Ar/^{39}Ar$ data (Table 2, Figs. 4, 5). Inverse isochrons were calculated separately for distinct phengite regions (cores, rims and mylonitic phengite) that potentially reflect distinct ages. In two cases, obvious outliers were a priori excluded (suspiciously young and old dates of ~69 Ma for MK-55-2 cores and ~111 Ma for MK-99-f, respectively). In addition to the MSWD value, we use the χ^2 test and determined the probability of occurrence (p) as statistical tools for evaluating the reliability of the inverse isochron age information (Table 2; see Baksi (1999, 2006) for details). If $p < 0.05$, excess scatter of data points relative to the expected scatter is demonstrated. If $p > 0.05$, the probability that the deviation from the expected result is due to chance only is 5% or more, which is generally considered as acceptable (Baksi, 2006).

For phengite cores in the weakly deformed EMS samples, there is a clear distinction in inverse isochron ages between the felsic gneisses (samples MK-30 and MK-55) and the micaschist (sample 3i). The gneisses yield inverse isochron ages of 82.6 ±0.6, 83.6 ±0.7, 84.8 ±0.7 and 85.0 ±3.3 Ma. All of the corresponding initial $^{40}Ar/^{36}Ar$ ratios are typically within 10% uncertainty of the atmospheric value (295.5) and/or overlap this value within error. MSWD values are moderate to high (1.9–4.7), but three of the four inverse isochrons yield p values <0.02. The inverse isochron ages show good agreement with average and weighted averages of single spot ages (Table 2). The small number of data points for the mafic gneiss (MK-52) renders the calculation of a reasonable inverse isochron impossible, but averages of single spots are similar to those determined from the two felsic gneisses. In contrast, the micaschist yields significantly younger inverse isochron ages of 75.8 ±0.9, 75.3 ±0.7 and 74.6 ±0.7 Ma. Two of those inverse isochrons result in relatively low MSWD values (1.6 and 1.8) associated with high p values (>0.09).

Inverse isochron ages derived for phengite rims of EMS samples are highly variable. Several very young ages, (52.4 ±4.6 Ma, 57.3 ±1.1 Ma, 60.2 ±1.4 Ma), more than 20 Ma younger than ages calculated for the cores, are linked to initial $^{40}Ar/^{36}Ar$ ratios that are much higher (>440) than the atmospheric ratio (295.5). In contrast, one relatively old inverse isochron age (88.7 ±1.1 Ma) results in a much lower initial $^{40}Ar/^{36}Ar$ ratio (207). Other inverse isochrons yield near-atmospheric initial $^{40}Ar/^{36}Ar$ ratios, and the corresponding ages (80.2 ±2.2 Ma, 77.1 ±1.1 Ma, 72.8 ±3.5 Ma) are slightly younger than the phengite core ages of the felsic gneisses but partly overlap with the core ages from the micaschist. The two phengite rim inverse isochrons, which yield ages that are similar to those from micaschist phengite cores, have fairly low MSWD (2.2 and 1.3) and high p values (0.11 and 0.25). Both of these were calculated for the felsic gneiss MK-55, which therefore has an average age difference between cores and rims of about 8 Ma.

No consistent age information is obtained for two discs of the mafic mylonite (sample MK-99). Inverse isochron ages are quite distinct (81.6 ±1.4 and 62.3 ±2.6 Ma), but both have initial $^{40}Ar/^{36}Ar$ ratios (417 and 954) well above the atmospheric value. Calculations result in moderately high MSWD (≥2.6) and rather low p values (≤0.01). In contrast, the tightly clustered group of apparent $^{40}Ar/^{39}Ar$ ages around 69–64 Ma from the felsic mylonite (sample TSZR) yields a well-defined inverse isochron age of 65.0 ±3.0 Ma with a $(^{40}Ar/^{36}Ar)_i$ ratio of 306 ±19, overlapping the atmospheric ratio (Fig. 5). The statistical parameters, MSWD = 1.0

and p = 0.392, point to a highly reliable age information. The six older dates from the felsic mylonite with a large scatter in apparent $^{40}Ar/^{39}Ar$ ages yield no statistically acceptable inverse isochron age.

6. Discussion

6.1. Significance of the $^{40}Ar/^{39}Ar$ ages

In situ laser spot analyses provide total gas ages for the individual spots, unlike step-heating analyses, where heterogeneities in the Ar isotopic composition may be identified by the release of different Ar components at different temperatures. Therefore, we constructed inverse isochron diagrams from spot analyses that are considered to represent identical ages in order to identify excess ^{40}Ar and potential effects of Ar loss. In inverse isochron diagrams, trapping of an excess ^{40}Ar component with a $^{36}Ar/^{40}Ar$ ratio lower than the atmospheric ratio (0.003384) causes displacement of data points to lower $^{36}Ar/^{40}Ar$ ratios (Kuiper, 2002). Since incorporation of excess ^{40}Ar is commonly heterogeneous (Sherlock and Kelley, 2002; Warren et al., 2011), scattering of data points is likely to occur, preventing the calculation of a precise inverse isochron. Argon loss, on the other hand, causes data points to move towards higher $^{39}Ar/^{40}Ar$ values because ^{39}Ar, which is produced in the nuclear reactor from ^{39}K, is not affected by Ar loss from the mineral (Kuiper, 2002). Hence, Ar loss will lead to younger apparent ages. If the Ar loss is complete, the timing of this event or the end of the Ar loss episode can be determined. However, if the Ar loss is incomplete, the inverse isochron age is geologically meaningless and will yield values between the initial age and the age when the Ar loss stopped (Kuiper, 2002).

$^{40}Ar/^{39}Ar$ ages in metamorphic rocks have traditionally been interpreted as cooling ages below the Ar closure temperature. However, a single closure temperature is unlikely to be applicable to metamorphism during rapid orogenic cycles (Warren et al., 2012a), which have presumably occurred in the SLZ (Rubatto et al., 2011). It is now established that recrystallization is the main Ar transfer mechanism within and between minerals in a metamorphic rock, and thermal diffusion is less important than fluid flow and deformation for isotope transport (Villa, 1998). Argon thermal diffusion in white mica is particularly inefficient in low-*T* and/or high-*P* regions, where Ar will be largely retained and little Ar is lost by thermal diffusion alone during exhumation (Warren et al., 2012a). Hence, $^{40}Ar/^{39}Ar$ ages from phengite in eclogite-facies rocks record crystallization and may even preserve discrete P-T stages and a record of the deformation history (Di Vincenzo et al., 2001; Putlitz et al., 2005; Warren et al., 2012b), but only where a zero-concentration of Ar can be demonstrated and excess ^{40}Ar is a negligible factor (Di Vincenzo et al., 2006; Warren et al., 2012a).

For the investigated samples from the SLZ, the presence of a fluid phase is prerequisite for sufficiently fast element transport that is necessary to cause the observed steep compositional gradients in phengite and amphibole and thermally induced volume diffusion as the main mechanism for the overprint can be excluded (Konrad-Schmolke et al., 2011a). Additional evidence for fluid-triggered compositional modifications comes from the observation that chemical re-equilibration in the EMS samples is restricted to fluid pathways, such as grain boundaries and brittle fractures.

6.1.1. Phengite cores in weakly deformed EMS samples

For all phengite cores, several data points show deviations from the best-fit inverse isochron. This scatter may be due to (i) mixing of Ar from relict and overprinted areas during analysis, (ii) excess ^{40}Ar incorporation, (iii) Ar loss, and (iv) different crystallization ages due to prolonged crystallization. Mixing of different crystal areas was avoided by conducting line analyses with total ablation depths ≤ 20 μm, which allowed for good spatial control on the sample surface and circumvented drilling through the desired region concerning depth. Initial $^{40}Ar/^{36}Ar$ ratios of the inverse isochrons are similar to the atmospheric ratio (Fig. 4, Table 2) so that there is no indication of a trapped excess ^{40}Ar component. There are also no systematic changes in apparent ages as a function of distance from the shear zone. Fossilized radiogenic Ar waves can occur on both regional and local scale related to different geological structures (Hyodo and York, 1993; Smith et al. 1994), but the similarity of apparent phengite core ages in three samples at variable distances from the shear zones argues against the presence of such a phenomenon, and the non-systematic age variation in relation to the distance from the shear zone is more likely related to fluid-mediated Ar diffusion properties of the rock (Baxter et al., 2002). Argon loss is a possible explanation for a few data points that plot to the right of the inverse isochron and yield relatively young apparent $^{40}Ar/^{39}Ar$ ages, but it is an unlikely explanation considering the predominantly smooth age distribution displayed by the data. Hence, we concluded that the deviation from the inverse isochron and the spread of apparent

$^{40}Ar/^{39}Ar$ ages was caused by an extended period of crystallization that lasted for several million years. Continuous recrystallization and/or resetting has also been advocated to explain a large variability in white mica $^{40}Ar/^{39}Ar$ ages (~14 Ma) from metamorphic rocks of the Attic-Cycladic belt (Bröcker et al., 2013), and similarly large spreads in ages, from a few Ma to ≥20 Ma, were reported from different parts of the Sanbagawa HP belt in Japan (Itaya et al., 2011). Based on the inverse isochron ages of the felsic gneisses, the minimal time span for the HP crystallization episode of the phengite cores in the EMS unit is from 88 to 82 Ma. The frequency distribution plot shows that apparent $^{40}Ar/^{39}Ar$ phengite core ages in the micaschist are distinctly younger. Although individual phengite core analyses of the gneisses and the micaschist overlap in age, the inverse isochrons of the micaschist confirm a distinctly younger period of (re)crystallization, lasting from ~77 to ~74 Ma.

Overlap of phengite $^{40}Ar/^{39}Ar$ ages with U-Pb and Lu-Hf geochronological data is often taken as evidence that $^{40}Ar/^{39}Ar$ ages record specific crystallization events and not cooling (Putlitz et al., 2005; Warren et al., 2012b). In the Sesia-Lanzo Zone and in particular for the EMS unit, a large number of Rb-Sr, $^{40}Ar/^{39}Ar$ and U/Th-Pb and Lu-Hf geochronological data have been obtained (Fig. 6; Inger et al., 1996; Reddy et al., 1996; Duchêne et al., 1997; Ruffet et al., 1995; 1997; Rubatto et al., 1999; 2011). The $^{40}Ar/^{39}Ar$ phengite core ages from the gneisses in the EMS are older than an U-Pb zircon age of 78.5 ±0.9 Ma that was interpreted to reflect the timing of HP metamorphism. They are also slightly older than the bulk of previously obtained laser spot $^{40}Ar/^{39}Ar$ ages (68–77 Ma), $^{40}Ar/^{39}Ar$ plateau ages (66-77 Ma) and total $^{40}Ar/^{39}Ar$ ages (65-79 Ma) (Ruffet et al., 1995; 1997; Inger et al., 1996). Beltrando et al. (2010) critically remark that published EMS $^{40}Ar/^{39}$ages older than 70 Ma are often considered as ‘anomalous’ and discarded as being related to excess ^{40}Ar, even when no assessment of the presence of such a component was performed. The inverse isochron ages in combination with the near-atmospheric $^{40}Ar/^{36}Ar$ ratios obtained from the inverse isochrons in this study indicates that these ages have geologic relevance. Moreover, overlap of the $^{40}Ar/^{39}Ar$ phengite core ages with an Rb-Sr isochron age of 85 ±1 Ma (Oberhänsli et al., 1985) and with U/Th-Pb allanite ages of ~85 ±2 Ma (Regis et al., in press) demonstrate that there was an episode of HP crystallization during that time. Phengite crystallization from 88–82 Ma is also consistent with $^{40}Ar/^{39}Ar$ ages of 92–82 Ma in detrital phengites from Tertiary sediments in the Piemonte Basin (Carrapa and Wijbrans, 2003).

The younger age of 77–74 Ma obtained from phengite cores of the micaschist point to full recrystallization several million years after the HP crystallization episode. This age is compatible with U-Pb zircon and U/Th-Pb allanite ages of 78.5 ±0.9, 76.8 ±0.9 and 75.6 ±0.8

Ma from EMS rocks (Rubatto et al., 2011) and a U-Pb zircon age of 76 ±1 Ma from a metamorphic vein within the EMS (Rubatto et al., 1999). Similar $^{40}Ar/^{39}Ar$ plateau ages were also obtained both in the EMS (73.6 ±0.3 to 76.9 ±0.6 Ma; Ruffet et al., 1995) and in the Pillonet Klippe (73.8 ±0.7 to 75.6 ±0.7 Ma; Cortiana et al., 1998), which structurally belongs to the SLZ. The location of the micaschist in the middle of our structural profile is incompatible with a P-T path that is significantly different to the other samples investigated. Instead, it suggests complete resetting of the Ar isotope system in the micaschist during fluid flow at HP conditions. The gneisses were less affected, most likely because the micaschist had a higher permeability that facilitated fluid flux. This scenario agrees well with the occurrence of a vein reported in Rubatto et al. (1998), in which zircon crystallized in equilibrium with a metamorphic fluid at the same time.

6.1.2. Overprinted phengite rims in weakly deformed EMS samples

It is evident from petrographic observations that the overprinted rims must have formed after phengite core crystallization, but inverse isochrons of the rims yield very inconsistent results (Fig. 4; Table 2). Some show relatively young inverse isochron ages (<60 Ma) coupled to $(^{40}Ar/^{36}Ar)_i$ values that are much higher than the atmospheric ratio (e.g. MK-30-1 and 3i-Ar6); others show ages that are higher than the respective core ages and have low $(^{40}Ar/^{36}Ar)_i$ values (e.g. MK-52-1). These features combined can best be explained by a combination of heterogeneous excess ^{40}Ar incorporation and Ar loss that prevented the extraction of reliable age information. The incorporation of excess ^{40}Ar is common in rocks with low permeability (Warren et al., 2012) and Ar depletion during low-T deformation is also a common phenomenon (Itaya et al., 2011). However, several inverse isochrons (e.g. MK-55-1, MK-55-2) provide statistically reliable ($p > 0.1$) ages of ~77–73 Ma with initial $^{40}Ar/^{36}Ar$ ratios close to the atmospheric ratio. This age is consistent with the metamorphic evolution of the rocks and interpreted to reflect a distinct episode of crystallization. It most likely represents a first phase of metamorphic overprint, which has been identified in EMS samples based on compositional modifications in omphacite, sodic amphibole and phengite (Konrad-Schmolke et al., 2011a).

Overprinted phengite rim ages of 77–73 Ma are similar to phengite core ages from the micaschist, supporting the view that complete resetting of the Ar isotope system in the micaschist was contemporaneous with a partial overprint in the less permeable gneisses. Crystallization ages of 75.6 ±0.8 Ma for allanite cores, 76.8 ±0.9 Ma for metamorphic zircon rims (Rubatto et al., 2011) and 76 ±1 Ma for vein zircon (Rubatto et al., 1999) support the interpretation of a distinct crystallization period during early exhumation of the EMS unit, as discussed in the preceding section. This first overprinting and recrystallization event must have occurred after HP crystallization at 88–82 Ma, but still at blueschist-facies conditions. The geochemical evidence for fluid-induced recrystallization of overprinted domains of the phengite grains is in excellent agreement with resetting of zircon ages and ensuing expulsion of radiogenic Pb due to fluid circulation (Gebauer and Grünenfelder, 1976). There is also evidence for later metasomatic fluid flow, presumably from the shear zone into the EMS country rocks. Phengite rims in the micaschist were affected by Ar loss, resulting in apparent $^{40}Ar/^{39}Ar$ ages <70 Ma down to ~57 Ma, and there is one apparent $^{40}Ar/^{39}Ar$ rim age of 64 ±8 Ma in a felsic gneiss (Electronic Annex). Later recrystallization and element redistribution is also indicated by the 63.6 ±0.8 Ma Rb-Sr isochron age derived from coexisting albite and phengite in the mafic gneiss (Babist et al., 2006), which indicates that a second metasomatic overprint has affected the weakly deformed EMS samples. Yet, this event was not strong enough to reset the Ar isotope system. The non-pervasive nature of the metasomatic alterations demonstrates that fluid flow and deformation were focused into the shear zone. Consequently, this second event significantly affected the relatively permeable rocks, such as the micaschist, whereas traces of this event are only sporadic in the gneisses.

6.1.3. Mylonitic phengite in samples from the Tallorno Shear Zone

Five analyses from the felsic mylonite (sample TSZR) with relatively young and tightly clustered apparent ages (64.7–68.8 Ma) form a well-defined inverse isochrons without any indication of excess ^{40}Ar that yields a statistically reliable $^{40}Ar/^{39}Ar$ age of 65.0 ±3.0 Ma (Fig. 5). These mylonitic phengites date recrystallization and fluid flow in the shear zone, representing a second phase of blueschist-facies overprint reflected in replacement of omphacite by blueschist-facies minerals (Konrad-Schmolke et al., 2011a). This age overlaps with U-Pb zircon ages from eclogitic micaschists (65 ±3 Ma and 66 ±1 Ma) and with a U-Pb zircon metamorphic rim age from an eclogite (65 ±5 Ma) in the EMS unit (Inger et al., 1996; Rubatto et al., 1999). A $^{40}Ar/^{39}Ar$ phengite plateau age of 65.9 ±0.4 Ma and concordant Rb-Sr phengite – whole rock isochron ages (64.2 ±2.5 Ma) were also interpreted as crystallization ages (Ruffet et al., 1997). They are also similar to the Rb-Sr isochron age of 63.6 ±0.8 Ma (Babist et al., 2006) and to several K-Ar ages between 61 ±4 and 63 ±3 Ma (Oberhänsli et al., 1985). The consistency of age data obtained by different methods provides strong evidence for a discrete event in the history of the SLZ causing crystallization of mylonitic phengite, zircon rims and albite (Fig. 6). Partial recrystallization occurred under blueschist-facies conditions and is related to deformation and shearing in the TSZ. These findings are in line with the significant influence of deformation on Ar diffusion by creating a network of fast diffusion pathways and causing a decrease in the effective length scale of Ar diffusion (Kramar et al., 2001; Mulch et al., 2002; Cosca et al., 2011). Ruffet et al. (1997) noted that closure of phengites to Ar loss in the EMS is ≤69.4 ±0.7 Ma, which fits well with an Ar loss event due to fluid flow and deformation in the TSZ at ~65 Ma, as determined in this study.

Six analyses with a range of apparent $^{40}Ar/^{39}Ar$ ages from 133 to 79 Ma and inconsistent inverse isochron ages in the felsic mylonite can also be explained by variable amounts of excess ^{40}Ar, either derived from relict phengite flakes or from a mixture of mylonitic and relict phengite (Fig. 5). These age variations of individual grains from a single hand specimen point to variations in the local Ar pressure and in the network of localized fluid (Hyodo and York, 1993).

Apparent $^{40}Ar/^{39}Ar$ ages in the mafic mylonite (sample MK-99) span a range of about 30 Ma, and the older dates of ~99 Ma and ~111 Ma clearly have experienced addition of excess ^{40}Ar, as is evident from displacement to lower $^{36}Ar/^{40}Ar$ ratios (Fig. 5). The $^{40}Ar/^{36}Ar$ ratio of the trapped Ar component, i.e. of the mixture of trapped atmospheric and excess Ar, is ~417 for disc MK-99-f. The obtained age of 81.6 ±1.6 Ma is not very well defined, but overlaps with phengite core crystallization ages in the EMS and hence suggests that most of the trapped excess ^{40}Ar is derived from the HP crystallization period. Although disc MK-99-DS yields an inverse isochron age (62.3 ±2.6 Ma) consistent with mylonitic phengite from the felsic mylonite, the lack of overlap between apparent $^{40}Ar/^{39}Ar$ spot ages and inverse isochron age combined with the poor statistical reliability of the inverse isochron (Table 2) render its reliability doubtful, and may instead be attributed to heterogeneous incorporation of excess ^{40}Ar.

6.2. Linking tracers of fluid flow (B, Li, $\delta^{11}B$) with $^{40}Ar/^{39}Ar$ data

Baxter et al. (2002) stressed that the diffusivity of Ar through an intergranular transport medium in different lithologies is the key aspect for the accumulation of excess ^{40}Ar. They introduced the parameter t_T, the transmissive timescale, which is the time for ^{40}Ar to escape through the local intergranular transporting medium to some sink for Ar. The transmissive timescale must be short relative to the timescale of local ^{40}Ar production to prevent an accumulation of excess ^{40}Ar. Only rock units with high Ar transmissivities, i.e. short transmissive timescales, will yield ages that are not affected by excess ^{40}Ar (Baxter et al., 2002). Rock units that are being deformed should, in general, be more amenable to dating as they provide pathways for fast Ar diffusion, which is increased by the presence of a fluid phase (Cosca et al., 2011; Kramar et al., 2001). In the Tallorno Shear Zone, deformation was accompanied by fluid flow (Babist et al., 2006; Konrad-Schmolke et al., 2011b), and hence other chemical tracers of fluid flow are expected to complement the results from the Ar isotopic analyses.

6.2.1. Limited fluid flow in the weakly deformed EMS unit

The low and highly negative $\delta^{11}B$ values of the phengite cores are consistent with preferential loss of ^{11}B during prograde dehydration and the resulting isotopically light B isotope signature in dehydrated rocks (Peacock and Hervig, 1999; Bebout, 1999; Wunder et al., 2005; Marschall et al., 2007). Although isotopic equilibration among nearby samples is expected because of fluid release by devolatilization reactions at peak pressures (Konrad-Schmolke et al., 2011a), the significant difference in $\delta^{11}B$ of ~8 ‰ between the phengite cores of the four EMS samples points to a lack of B isotopic equilibration on the km scale and limited pervasive fluid flow during phengite crystallization at HP conditions. This agrees well with previous observations of limited fluid flow during subduction in the internal parts of the SLZ (Konrad-Schmolke et al., 2006). The lower B contents in phengite cores of the micaschist point to equilibration with larger amounts of fluid compared to the gneisses, since the fluid-mobile B is a sensitive indicator for effects of fluid equilibration in the weakly deformed EMS samples (Konrad-Schmolke et al., 2011b). However, significant influx of external, slab-derived fluids, which should result in increasing $\delta^{11}B$ values, is excluded for this first overprinting stage (~77–73 Ma) because the B isotopic composition of the micaschist falls into the middle of the range exhibited by the gneisses. Hence, phengite core crystallization in the micaschist is largely dominated by redistribution of B due to percolation of internally derived fluids (Fig. 7), suggesting that external fluids associated with deformation and fluid flow in the TSZ did not play a significant role during this stage.

This first fluid-induced overprint (~77–73 Ma) also led to a partial compositional re-equilibration and the formation of the metasomatized phengite and amphibole rims in the EMS gneisses (Fig. 7; Konrad-Schmolke et al., 2011a, b). Thermodynamic modeling shows that the presence of a fluid is required to produce the observed mineral assemblages and mineral chemical modifications on the retrograde *P-T* path. The overlap in $\delta^{11}B$ values of relict cores and overprinted rims is consistent with an internally derived fluid, as already deduced from the micaschist phengite cores that recrystallized contemporaneously. Internally derived retrograde fluids in HP metasediments can be liberated by a reduction of modal white mica (Heinrich, 1982). The release of internally derived fluids is also permitted by thermodynamic models in those regions where the retrograde *P-T* path crosses successively decreasing isopleths of water content bound in minerals. The observed depletion of B and Li in the phengite rims (Fig. 3) is consistent with this scenario because both Li and B prefer paragonite over phengite (Marschall et al., 2006a), so that paragonite growth contemporaneous with the formation of phengite rims (Fig. 2d) would cause a relative depletion of Li and B in the phengite rims as compared to the corresponding cores. Paragonite in our samples contains ~100-120 μg/g B, consistent with this interpretation. Lithium concentrations in paragonite are ~45 μg/g Li, broadly similar to phengite, but Li is also preferentially incorporated into newly formed amphibole rims during the overprint. On the other hand, the influence of an external fluid is indicated at least for the mafic gneiss that shows a small B isotopic difference (on average ~3‰) between phengite cores and rims. This external fluid influx is consistent with the typical lack of retrograde devolatilization reactions in mafic eclogites (Heinrich, 1982). Results from thermodynamic modeling point to a larger amount of water influx into the mafic gneiss as compared to the felsic samples during retrograde metamorphism (Konrad-Schmolke et al, 2011a).

The very low fluid/rock ratios that were calculated for the first metasomatic overprint in the EMS samples (Konrad-Schmolke et al., 2011b) indicate that very little, if any, fluid left the rock volume, independent of the exact proportions of internally and externally derived fluids (Fig. 7). The rocks seem to have acted as a sponge, absorbing any fluid diverted from the TSZ into the EMS country rocks and mixing it with internally produced dehydration-derived fluids. The limited alteration of the B isotopic compositions agree well with limited fluid influx, although some redistribution of B and Li occurred during metasomatic overprinting. Changes in X_{Mg} and Si content of phengite (Fig. 2c, d) are in agreement with fluid-induced recrystallization as these parameters not only depend on changes in *P-T* conditions, but also on fluid availability and the phase assemblage during recrystallization. Hence, oscillatory major-element zonation in phengite can be explained by changes in fluid availability and cannot be taken as unequivocal evidence for periodic changes in lithostatic pressure and “yo-yo tectonics” in the SLZ (Rubatto et al., 2011). Fluid-controlled phengite recrystallization is supported by the observed incorporation of excess ^{40}Ar in some of the rims. Ar transmissivity remained low where little or no fluid escaped from the rock, and any available excess ^{40}Ar could have been redistributed into the rims.

6.2.2. Extensive fluid flow in the Tallorno Shear Zone

The mylonitic samples from the TSZ have the highest $\delta^{11}B$ values of all investigated samples and show no isotopic core-rim zonation. This is consistent with the strong major element re-equilibration and considerable leaching of B and Li during the mylonitic overprint and the associated fluid influx (Fig. 7). The estimated $\delta^{11}B_{fluid}$ of +7 ±4 ‰ is similar to estimates of slab-derived fluids that entered exhuming HP rocks based on tourmaline compositions (Bebout and Nakamura, 2003; Altherr et al., 2004; Marschall and Jiang, 2011). The high-$\delta^{11}B$ composition of these fluids either reflects subducting altered oceanic materials or forms by fluid-rock interaction of slab-derived fluids with material in the exhumation channel during the retrograde evolution (Marschall et al., 2006b; 2009). The observed high $\delta^{11}B$ values, therefore, fit well with the geological setting of SLZ, which was located above the subducting Piemonte Ocean at that time.

The difference in $\delta^{11}B$ between EMS phengite rims and TSZ mylonitic phengites can be explained by a different origin and/or a relatively B-poor nature of the fluid. The different origin is not in contrast to the similar major elemental composition of EMS phengite rims and TSZ mylonitic phengite, because the presence of a fluid and the same degree of water-saturation play the major role in determining the phengite compositions at the same *P-T* conditions, independent of the fluid origin. If the shear zone fluid interacted with the phengite rims, its presumed B-poor nature (25 mg/g; Konrad-Schmolke et al., 2011b) would be in agreement with most B in the rims being inherited from the phengite cores during the metasomatic overprint. The combination of distinct $\delta^{11}B$ values and different $^{40}Ar/^{39}Ar$ ages demonstrates that two different stages in the metamorphic-metasomatic evolution of this SLZ are recorded. The B isotopic composition of the TSZ fluid, during the second metasomatic overprint, was externally controlled, whereas in the EMS there was only limited fluid flow during the first metasomatic overprint, and the fluid composition was internally controlled by the rock composition. Rb-Sr data (Babist et al., 2006) bear evidence that the EMS samples have at least partly been affected by fluid-rock interaction and elemental exchange during fluid flow and deformation in the shear zone at ~65 Ma. However, this event did not significantly affect the Ar and B isotope systematics.

Although B concentrations and $\delta^{11}B$ are similar for the felsic and mafic mylonites, the mafic mylonite (MK-99) lacks any record of the younger events at 65.0 ±3.0 Ma observed in the felsic mylonite. Ages and excess ^{40}Ar contents are lithologically correlated, as observed in other studies where different ages in spatially adjacent rocks were observed (Baxter et al., 2002). The young age in the felsic mylonite indicates short transmissive timescales for Ar. Any inherited ^{40}Ar was transported away before the mylonitic phengite was closed to Ar exchange. Yet, the scattered older apparent $^{40}Ar/^{39}Ar$ ages (133–79 Ma) demonstrate that this transport was not complete. A total lack of apparent $^{40}Ar/^{39}Ar$ ages around 65 Ma coupled to a significant build-up of excess ^{40}Ar is observed in the mafic mylonite. This observation, which is apparently contradicting the re-equilibrated $\delta^{11}B$ values, can be explained by exposure of the mafic mylonite to a grain boundary fluid with high concentrations of excess ^{40}Ar, as indicated by the high $^{40}Ar/^{36}Ar$ ratio of the trapped Ar. Thus, the apparent ages in the mafic mylonite depend on the concentration of excess ^{40}Ar and/or the extent to which the $^{40}Ar/^{36}Ar$ ratio is greater than the atmospheric ratio in the fluid in equilibrium with the growing phengite. A similar mechanism was proposed to explain rim ages that were older than core ages in zoned minerals (Warren et al., 2011). Here, B and Ar isotopes provide complementary information.

7. Conclusions

Using *in situ* UV laser $^{40}Ar/^{39}Ar$ dating, we identified three distinct age periods from partially overprinted white mica in eclogitic micaschists and mylonites from the Sesia-Lanzo Zone, Western Alps. By combining the $^{40}Ar/^{39}Ar$ data with B elemental and isotopic analyses, we linked the age information to fluid-rock interaction processes. Phengite core crystallization in gneisses from the EMS unit is constrained to 88–82 Ma, a few million years older than previous estimates of peak *P*-*T* conditions based on U-Pb zircon geochronology (Rubatto et al., 2011), but consistent with Rb-Sr isochron data (Oberhänsli et al., 1985). The variation in $\delta^{11}B$ among the phengite cores demonstrates a lack of B isotopic equilibration on the km scale at peak metamorphic conditions. For the petrographically and chemically distinct phengite rims, younger crystallization ages of 77–73 Ma were obtained. Although there is evidence for incorporation of excess ^{40}Ar and Ar loss in some samples, this age agrees well with crystallization ages of metamorphic zircon rims and vein zircon (Rubatto et al., 1999; 2011).

The lower B contents observed in the rims also occur in phengite cores of a micaschist, and both yield similar $^{40}Ar/^{39}Ar$ ages. Together, they date a first period of metasomatic overprint in the EMS. The fluid composition during this overprint was largely internally controlled, as demonstrated by the B data, and B was redistributed among the recrystallizing minerals. Crystallization of mylonitic phengite in the Tallorno Shear Zone occurred at 65.0 ±3.0 Ma. In agreement with high fluid/rock ratios determined for the TSZ, the B isotopic composition of the TSZ fluid ($\delta^{11}B$ = +7 ±4 ‰) was externally controlled. In summary, the combined Ar and B isotopic data are accurate enough to discriminate several tectonometamorphic events. The distribution of apparent $^{40}Ar/^{39}Ar$ ages suggests episodes of HP crystallization and metasomatic overprinting, lasting several millions of years, rather than discrete events of less than one million year duration. Phengite crystallization periods can be related to fluid flow and deformation along the *P-T* path experienced by the SLZ rocks.

Acknowledgments

We thank Christine Fischer for help with sample preparation and Fritz Falkenau and Susanne Schneider for support during SIMS measurements. We also thank the associate editor for editorial handling and helpful advice, and three anonymous reviewers for their detailed and constructive comments, which helped to improve the manuscript. Funding of this work by the Deutsche Forschungsgemeinschaft (grant KO-3750/2-1) is gratefully acknowledged.

References

Altherr R., Topuz G., Marschall H., Zack T., Ludwig T. (2004) Evolution of a tourmaline-bearing lawsonite eclogite from the Elekdağ area (Central Pontides, N Turkey): evidence for infiltration of slab-derived B-rich fluids during exhumation. *Contrib. Mineral. Petrol.* **148**, 409-425.

Arnaud N.O., Kelley S.P. (1995) Evidence for excess argon during high pressure metamorphism in the Dora Maira Massif (western Alps, Italy), using an ultra-violet laser ablation microprobe ^{40}Ar-^{39}Ar technique. *Contrib. Mineral. Petrol.* **121**, 1-11.

Babist J., Handy M.R., Konrad-Schmolke M., Hammerschmidt K. (2006) Precollisional, multistage exhumation of subducted continental crust: The Sesia Zone, western Alps. *Tectonics* **25**, TC6008, doi:10.1029/2005TC001927.

Baksi A.K. (1999) Reevaluation of plate motion models based on hotspot tracks in the Atlantic and Indian Oceans. *J. Geol*. **107**, 13-26.

Baksi A.K. (2006) Guidelines for assessing the reliability of ^{40}Ar/^{39}Ar plateau ages: Application to ages relevant to hotspot tracks. http://www.mantleplumes.org/ArAr.html.

Baxter E.F., DePaolo D.J., Renne P.R. (2002) Spatially correlated anomalous ^{40}Ar/^{39}Ar "age" variations in biotites about a lithologic contact near Simplon Pass, Switzerland: A mechanistic explanation for excess Ar. *Geochim. Cosmochim. Acta* **66**, 1067-1083.

Bebout G.E., Nakamura E. (2003) Record in metamorphic tourmalines of subduction-zone devolatilization and boron cycling. *Geology* **31**, 407-410.

Bebout G.E., Ryan J.G., Leeman W.P., Bebout A.E. (1999) Fractionation of trace elements by subduction-zone metamorphism – effect of convergent-margin thermal evolution. *Earth Planet. Sci. Lett*. **171**, 63-81.

Beltrando M., Compagnoni R., Lombardo B. (2010) (Ultra-) High-pressure metamorphism and orogenesis: An Alpine perspective. *Gondwana Res.* **18**, 147-166.

Beltrando M., Lister G.S., Forster M., Dunlap W.J., Fraser G., Hermann J. (2009) Dating microstructures by the ^{40}Ar/^{39}Ar step-heating technique: Deformation-pressure-temperature-time history of the Penninic Units of the Western Alps. *Lithos* **113**, 801-819.

Boundy T.M., Hall C.M., Li G., Essene E.J., Halliday A.N. (1997) Fine-scale isotopic heterogeneities and fluids in the deep crust: a ^{40}Ar/^{39}Ar laser ablation and TEM study of muscovites from a granulite-eclogite transition zone. *Earth Planet. Sci. Lett*. **148**, 223-242.

Brenan J.M., Ryerson F.J., Shaw H.F. (1998) The role of aqueous fluids in the slab-to-mantle transfer of boron, beryllium, and lithium during subduction: experiments and models. *Geochim. Cosmochim. Acta* **62**, 3337-3347.

Bröcker M., Baldwin S., Arkudas R. (2013) The geological significance of 40Ar/39Ar and Rb-Sr white mica ages from Syros and Sifnos, Greece: a record of continuous (re)crystallization during exhumation? *J. metamorphic Geol*. **31**, 629-646.

Carrapa B., Wijbrans J. (2003) $^{40}Ar/^{39}Ar$ detrital mica ages in Tertiary sediments shed a new light on the Eo-Alpine evolution. *J. Virtual Explor.* **13**, 43-55.

Catanzaro F.J., Champion C.E., Garner E.L., Marinenko G., Sappenfield K.M., Shields W.R. (1970) Boric acid: isotopic and assay standard reference materials. *Natl. Bur. Stand. Spec. Publ.* **260**, 1-70.

Channell J.E.T., Hodell D.A., Singer B.S., Xuan C. (2010) Reconciling astrochronological and $^{40}Ar/^{39}Ar$ ages for the Matuyama-Brunhes boundary and late Matuyama Chron. *Geochem. Geophys. Geosyst.* **11**, doi:10.1029/2010GC003203.

Cortiana G., Dal Piaz G.V., Del Moro A., Hunziker J.C., Martin S. (1998) ^{40}Ar-^{39}Ar and Rb-Sr dating of the Pillonet klippe and Sesia-Lanzo basal slice in the Ayas valley and evolution of the Austroalpine-Piedmont nappe stack. *Mem. Sci. Geol.* **50**, 177-194.

Cosca M., Stünitz H., Bourgeix A.-L., Lee J.P. (2011) $^{40}Ar^*$ loss in experimentally deformed muscovite and biotite with implications for $^{40}Ar/^{39}Ar$ geochronology of naturally deformed rocks. *Geochim. Cosmochim. Acta* **75**, 7759-7778.

Di Vincenzo G., Palmeri R. (2001) An ^{40}Ar-^{39}Ar investigation of high-pressure metamorphism and the retrogressive history of mafic eclogites from the Lanterman Range (Antarctica): evidence against a simple temperature control on argon transport in amphibole. *Contrib. Mineral. Petrol.* **141**, 15-35.

Di Vincenzo G., Ghiribelli B., Giorgetti G., Palmeri R. (2001) Evidence of a close link between petrology and isotope records: constraints from SEM, EMP, TEM and in situ ^{40}Ar-^{39}Ar laser analyses on multiple generations of white micas (Lanterman Range, Antarctica). *Earth Planet. Sci. Lett*. **192**, 389-405.

Di Vincenzo G., Carosi R., Palmeri R. (2004) The relationship between tectono-metamorphic evolution and argon isotope records in white mica: constraints from *in situ* ^{40}Ar-^{39}Ar laser analysis of the Variscan basement of Sardinia. *J. Petrol*. **45**, 1013-1043.

Di Vincenzo G., Tonarini S., Lombardo B., Castelli D., Ottolini L. (2006) Comparison of ^{40}Ar-^{39}Ar and Rb-Sr data on phengites from the UHP Brossasco-Isasca unit (Dora Maira Massif, Italy): Implications for dating white mica. *J. Petrol*. **47**, 1439-1465.

Duchêne S., Blichert-Toft J., Luais B., Télouk P., Lardeaux J.-M., Albarède F. (1997) The Lu-Hf dating of garnets and the ages of the Alpine high-pressure metamorphism. *Nature* **387**, 586-589.

Früh-Green G., Scambelluri M., Vallis F. (2001) O-H isotope ratios of high-pressure ultramafic rocks: Implications for fluid sources and mobility in the subducted hydrous mantle. *Contrib. Mineral. Petrol*. **141**, 145-159.

Gebauer D., Grünenfelder M. (1976) U-Pb zircon and Rb-Sr whole rock dating of low-grade metasediments – Example: Montagne Noire (southern France). *Contrib. Mineral. Petrol.* **59**, 13-32.

Giorgis D., Cosca M., Li S. (2000) Distribution and significance of extraneous argon in UHP eclogite (Sulu terrain, China): insight from in situ $^{40}Ar/^{39}Ar$ UV-laser ablation analysis. *Earth Planet. Sci. Lett*. **181**, 605-615.

Hacker B.R., Wang Q. (1995) Ar/Ar geochronology of ultrahigh-pressure metamorphism in central China. *Tectonics* **14**, 994-1006

Halama R., John T., Herms P., Hauff F., Schenk V. (2011) A stable (Li, O) and radiogenic (Sr, Nd) isotope perspective on metasomatic processes in a subducting slab. *Chem. Geol*. **281**, 151-166.

Hames W.E., Cheney J.T. (1997) On the loss of $^{40}Ar^*$ from muscovite during polymetamorphism. *Geochim. Cosmochim. Acta* **61**, 3863-3872.

Heinrich C.A. (1982) Kyanite-eclogite to amphibolite facies evolution of hydrous mafic and pelitic rocks, Adula Nappe, Central Alps. *Contrib. Mineral. Petrol.* **81**, 30-38.

Hess J.C., Lippolt H.J. (1994) Compilation of K-Ar measurements on HD-B1 standard biotite – 1994 status report. In *Phanerozoic Time Scale (ed. G.S. Odin), Bull. Liais. Inform. IUGS Subcomm. Geochronol.* ***12**, 19-23.*

Hyodo H., York D. (1993) The discovery and significance of a fossilized radiogenic argon wave (argonami) in the Earth's crust. *Geophys. Res. Lett.* **20**, 61-64.

Inger S., Ramsbotham W., Cliff R.A., Rex D.C. (1996) Metamorphic evolution of the Sesia-Lanzo Zone, Western Alps: time constraints from multi-system geochronology. *Contrib. Mineral. Petrol.* **126**, 152-168.

Ishikawa T., Nakamura E. (1994) Origin of the slab component in arc lavas from across-arc variation of B and Pb isotopes. *Nature* **370**, *205-208*.

Ishizuka O. (1998) Vertical and horizontal variations of the fast neutron flux in a single irradiation capsule and their significance in the laser-heating $^{40}Ar/^{39}Ar$ analysis: Case study for the hydraulic rabbit facility of the JMTR reactor, Japan. *Geochem. J.* **32**, 243-252,

Itaya T., Tsujimori T., Liou J.G. (2011) Evolution of the Sanbagawa and Shimanto high-pressure belts in SW Japan: Insights from K-Ar (Ar-Ar) geochronology. *J. Asian Earth Sci.* **42**, 1075-1090.

Kelley S. (2002) Excess argon in K-Ar and Ar-Ar geochronology. *Chem. Geol*. **188**, 1-22.

Klemme S., Marschall, H.R., Jacob D.E., Prowatke S., Ludwig T. (2011) Trace-element partitioning and boron isotope fractionation between white mica and tourmaline. *Can. Mineral.* **49**, 165-176.

Konrad-Schmolke M., Babist J., Handy M.R., O'Brien P.J. (2006) The physico-chemical properties of a subducted slab from garnet zonation patterns (Sesia Zone, Western Alps). *J. Petrol*. **47**, 2123-2148.

Konrad-Schmolke M., O'Brien P.J., Zack T. (2011a) Fluid migration above a subducted slab – constraints on amount, pathways and major element mobility from partially overprinted eclogite-facies rocks (Sesia Zone, Western Alps). *J. Petrol.* **52**, 457-486.

Konrad-Schmolke M., Zack T., O'Brien P., Barth M. (2011b) Fluid migration above a subducted slab – thermodynamic and trace element modelling of fluid-rock interaction in partially overprinted eclogite-facies rocks (Sesia Zone, Western Alps). *Earth Planet. Sci. Lett.* **311**, 287-298.

Kramar N., Cosca M.A., Hunziker J.C. (2001) Heterogeneous 40Ar* distributions in naturally deformed muscovite: in situ UV-laser ablation evidence for microstructurally controlled intragrain diffusion. *Earth Planet. Sci. Lett.* **192**, 377-388.

Kuiper Y.D. (2002) The interpretation of inverse isochron diagrams in $^{40}Ar/^{39}Ar$ geochronology. *Earth Planet. Sci. Lett.* **203**, 499-506.

Kuiper K.F., Deino A., Hilgen F.J., Krijgsman W., Renne P.R., Wijbrans J.R. (2008) Synchronizing rock clocks of Earth history. *Science* **320**, 500-504.

Lanphere, M.A. (2004) Reply to comment on ''Precise K–Ar, $^{40}Ar/^{39}Ar$, Rb–Sr and U–Pb mineral ages from the 27.5 Ma Fish Canyon Tuff reference standard'' by M.A. Lanphere and H. Baadsgaard. *Chem. Geol.* **211**, 389–390.

Lanphere M.A., Baadsgaard H. (2001) Precise K-Ar, $^{40}Ar/^{39}Ar$, Rb-Sr and U/Pb mineral ages from the 27.5 Ma Fish Canyon Tuff reference standard. *Chem. Geol.* **175**, 653-671.

Lanphere M. A., Dalrymple G.B. (2000) First-principles calibration of ^{38}Ar tracers: Implications for ages of $^{40}Ar/^{39}Ar$ fluence monitors: *U.S. Geological Survey Professional Paper* **1621**, 1-10.

Lee J.-Y., Marti K., Severinghaus J.P., Kawamura K., Yoo H.-S., Lee J.B., Kim J.S. (2006) A redetermination of the isotopic abundances of atmospheric Ar. *Geochim. Cosmochim. Acta* **70**, 4507-4512.

Marschall H.R., Altherr R., Ludwig T., Kalt A., Gméling K., Kasztovszky Z. (2006a) Partitioning and budget of Li, Be and B in high-pressure metamorphic rocks. *Geochim. Cosmochim. Acta* **70**, 4750-4769.

Marschall H.R., Ludwig T., Altherr R., Kalt A., Tonarini S. (2006b) Syros metasomatic tourmaline: evidence for very high-$\delta^{11}B$ fluids in subduction zones. *J. Petrol.* **47**, 1915-1942.

Marschall H.R., Altherr R., Rüpke L. (2007) Squeezing out the slab – modelling the release of Li, Be and B during progressive high-pressure metamorphism. *Chem. Geol.* **239**, 323-335.

Marschall H.R., Korsakov A.V., Luvizotto G.L., Nasdala L., Ludwig T. (2009) On the occurrence and boron isotopic composition of tourmaline in (ultra)high-pressure metamorphic rocks. *J. Geol. Soc., London* **166**, 811-823.

Marschall H.R., Jiang S.Y. (2011) Tourmaline isotopes: no element left behind. *Elements* **7**, 313-319.

McDougall I., Harrison T.M (1999) Geochronology and thermochronology by the $^{40}Ar/^{39}Ar$ method. Oxford University Press, New York.

Mulch A., Cosca M.A., Handy M.R. (2002) In-situ UV-laser $^{40}Ar/^{39}Ar$ geochronology of a micaceous mylonite: an example of defect-enhanced argon loss. *Contrib. Mineral. Petrol*. **142**, 738-752.

Nier A.O. (1950) A redetermination of the relative abundances of the isotopes of carbon, nitrogen, oxygen, argon, and potassium. *Phys. Rev.* **77**, 789-793.

Oberhänsli R., Hunziker J.C., Martinotti G., Stern W.B. (1985) Geochemistry, geochronology and petrology of Monte Mucrone: An example of eo-Alpine eclogitization of Permian granitoids in the Sesia-Lanzo Zone, Western Alps, Italy. *Chem. Geol. (Isot. Geosci. Sect.)* **52**, 165-184.

Pabst S., Zack T., Savov I.P., Ludwig T., Rost D., Tonarini S., Vicenzi E.P. (2012) The fate of subducted oceanic slabs in the shallow mantle: Insights from boron isotopes and light element composition of metasomatized blueschists from the Mariana forearc. *Lithos* **132-133**, 162-179.

Peacock S.M., Hervig R.L. (1999) Boron isotopic composition of subduction-zone metamorphic rocks. *Chem. Geol*. **160**, 281-290.

Putlitz, B, Matthews A., Valley J.W. (2000) Oxygen and hydrogen isotope study of high-pressure metagabbros and metabasalts (Cyclades, Greece): implications for the subduction of oceanic crust. *Contrib. Mineral. Petrol*. **138**, 114-126.

Putlitz B., Cosca M.A., Schumacher J.C. (2005) Prograde mica $^{40}Ar/^{39}Ar$ growth ages recorded in high pressure rocks (Syros, Cyclades, Greece). *Chem. Geol*. **214**, 79-98.

Reddy S.M., Kelley S.P., Wheeler J. (1996) A $^{40}Ar/^{39}Ar$ laser probe study of micas from the Sesia Zone, Italian Alps: implications for metamorphic and deformation histories. *J. metamorphic Geol.* **14**, 493-508.

Regis D., Rubatto D., Darling J., Cenci-Tok B., Zucali M, Engi M. (2013) Multiple metamorphic stages within an eclogite-facies terrane (Sesia Zone, Western Alps) revealed by U/Th-Pb petrochronology. *J. Petrol.,* in press.

Renne P. R., Mundil R., Balco G., Min K., Ludwig K.R. (2010) Joint determination of ^{40}K decay constants and $^{40}Ar^{*}/^{40}K$ for the Fish Canyon sanidine standard, and improved accuracy for $^{40}Ar/^{39}Ar$ geochronology. *Geochim. Cosmochim. Acta* **74**, 5349-5367.

Renne P.R., Swisher C.C., Deino A.L., Karner D.B., Owens T.L., DePaolo D.J. (1998) Intercalibration of standards, absolute ages and uncertainties in $^{40}Ar/^{39}Ar$ dating. *Chem. Geol.* **145**, 117-152.

Rosner M., Erzinger J., Franz G., Trumbull R.B. (2003) Slab-derived boron isotope signatures in arc volcanic rocks from the Central Andes and evidence for boron isotope fractionation during progressive slab dehydration. *Geochem. Geophys. Geosyst* **4**, doi:10.1029/2002GC000438.

Rosner M., Wiedenbeck M., Ludwig T. (2008) Composition-induced variations in SIMS instrumental mass fractionation during boron isotope ratio measurements of silicate glasses. Geostand. Geoanal. Res. **32**, 27-38.

Rubatto D., Gebauer D., Compagnoni R. (1999) Dating of eclogite-facies zircons: the age of Alpine metamorphism in the Sesia-Lanzo Zone (Western Alps). *Earth Planet. Sci. Lett*. **167**, 141-158.

Rubatto D., Regis D., Hermann J., Boston K., Engi M., Beltrando M., McAlpine S.R.B. (2011) Yo-yo subduction recorded by accessory minerals in the Italian Western Alps. *Nature Geosci*. **4**, 338-342.

Ruffet G., Féraud G., Ballèvre M., Kiénast J.-R. (1995) Plateau ages and excess argon in phengites: an ^{40}Ar-^{39}Ar laser probe study of Alpine micas (Sesia Zone, Western Alps, northern Italy). *Chem. Geol. (Isot. Geosci. Sect.)* **121**, 327-343.

Ruffet G., Gruau G., Ballèvre M., Féraud G., Philippot P. (1997) Rb-Sr and ^{40}Ar-^{39}Ar laser probe dating of high-pressure phengites from the Sesia zone (Western Alps): underscoring of excess argon and new age constraints on the high-pressure metamorphism. *Chem. Geol.* **141**, 1-18.

Scaillet S. (1996) Excess ^{40}Ar transport scale and mechanism in high-pressure phengites: A case study from an eclogitized metabasite of the Dora-Maira nappe, western Alps. *Geochim. Cosmochim. Acta* **60**, 1075-1090.

Scaillet S., Féraud G., Lagabrielle Y., Ballèvre M., Ruffet G. (1990) ^{40}Ar/^{39}Ar laser-probe dating by step heating and spot fusion of phengites from the Dora Maira nappe of the western Alps, Italy. *Geology* **18**, 741-744.

Scherer E., Münker C., Mezger K. (2001) Calibration of the lutetium-hafnium clock. Science **293**, 683-687.

Schwarz W.H., Trieloff M. (2007) Intercalibration of ^{40}Ar-^{39}Ar age standards NL-25, HB3gr hornblende, GA1550, SB-3, HD-B1 biotite and BMus/2 muscovite. *Chem. Geol*. **242**, 218-231.

Sherlock S.C., Arnaud N.O. (1999) Flat plateau and impossible isochrons: Apparent ^{40}Ar-^{39}Ar geochronology in a high-pressure terrain. *Geochim. Cosmochim. Acta* **63**, 2835-2838.

Sherlock S., Kelley S. (2002) Excess argon evolution in HP-LT rocks: a UVLAMP study of phengite and K-free minerals, NW Turkey. *Chem. Geol*. **182**, 619-636.

Smith P.E., York D., Easton R.M., Özdemir Ö., Layer P.W. (1994) A laser ^{40}Ar-^{39}Ar study of minerals across the Grenville Front: investigation of reproducible excess Ar patterns. *Can. J. Earth Sci*. **31**, 808-817.

Sudo M., Uto K., Anno K., Ishizuka O., Uchiumi S. (1998) SORI93 biotite: A new mineral standard for K-Ar dating. *Geochem. J.* **32**, 49-58.

Trumbull R., Krienitz M.-S., Grundmann G., Wiedenbeck M. (2009) Tourmaline geochemistry and $\delta^{11}B$ variations as a guide to fluid-rock interaction in the Habachtal emerald deposit, Tauern Window, Austria. *Contrib. Mineral. Petrol*. **157**, 411-427.

Uto K., Ishizuka O., Matsumoto A., Kamioka H., Togashi S. (1997) Laser-heating $^{40}Ar/^{39}Ar$ dating system of the Geological Survey of Japan: System outline and preliminary results. *Bull. Geol. Surv. Japan* **48**, 23-46.

Venturini G., Martinotti G., Armando G., Barbero M., Hunziker J.C. (1994) The Central Sesia Lanzo Zone (Western Italian Alps): new field observations and lithostratigraphic subdivisions. *Schweiz. Mineral. Petrograph. Mitt*. **74**, 115-125.

Villa I. (1998) Isotopic closure. *Terra Nova* **10**, 42-47.

Warren C.J., Sherlock S.C., Kelley S.P. (2011) Interpreting high-pressure phengite $^{40}Ar/^{39}Ar$ laserprobe ages: an example from Saih Hatat, NE Oman. *Contrib. Mineral. Petrol*. **161**, 991-1009.

Warren C.J., Hanke F., Kelley S.P. (2012a) When can muscovite $^{40}Ar/^{39}Ar$ dating constrain the timing of metamorphic exhumation? *Chem. Geol*. **291**, 79-86.

Warren C.J., Kelley, S.P., Sherlock S.C., McDonald C.S. (2012b) Metamorphic rocks seek meaningful cooling rate: Interpreting $^{40}Ar/^{39}Ar$ ages in an exhumed ultra-high pressure terrane. *Lithos* **155**, 30-48.

Warren C.J., Smye A.J., Kelley S.P., Sherlock S.C. (2012c) Using white mica $^{40}Ar/^{39}Ar$ data as a tracer for fluid flow and permeability under high-P conditions: Tauern Window, Eastern Alps. *J. metamorphic Geol*. **30**, 63-80.

Wiederkehr M., Sudo M., Bousquet R., Berger A., Schmid S.M. (2009) Alpine orogenic evolution from subduction to collisional thermal overprint: The $^{40}Ar/^{39}Ar$ age constraints from the Valaisan Ocean, central Alps. *Tectonics* **28**, TC6009, doi:10.1029/2009TC002496.

Wilke F. D. H., O'Brien P.J., Gerdes G., Timmerman M.J., Sudo M., Khan M.A. (2010) The multistage exhumation history of the Kaghan Valley UHP series, NW Himalaya, Pakistan from U-Pb and $^{40}Ar/^{39}Ar$ ages. *Eur. J. Mineral.* **22**, 703-719.

Willner A.P., Sepúlveda F.A., Hervé F., Massonne H.-J., Sudo, M. (2009) Conditions and timing of pumpellyite-actinolite facies metamorphism in the early Mesozoic frontal accretionary prism of the Madre de Dios Archipelago (latitude 50°20'S; Southern Chile). *J. Petrol*. **50**, 2127-2155.

Willner A.P., Massonne H.-J., Ring U., Sudo M., Thomson S.N. (2011) P-T evolution and timing of a late Palaeozoic fore-arc system and its heterogeneous Mesozoic overprint in north-central Chile (latitudes 31-32°S). *Geol. Mag*. **149**, 177-207.

Wunder B., Meixner A., Romer R.L., Wirth R., Heinrich W. (2005) The geochemical cycle of boron: Constraints from boron isotope partitioning experiments between mica and fluid. *Lithos* **84**, 206-216.

Figure captions:

Fig. 1: (a) Simplified geological map of the Western Alps with the Sesia-Lanzo Zone (modified from Beltrando et al., 2010). DB = Dent Blanche, DM = Dora Maira, GP = Gran Paradiso, IZ = Ivrea Zone, MR = Monte Rosa, SCZ = Strona-Ceneri Zone, SLZ = Sesia-Lanzo Zone. (b) Schematic sampling profile in the Sesia-Lanzo Zone from the Tallorno Shear Zone (TSZ) into the EMS unit along the Chiusella Valley (modified from Konrad-Schmolke et al., 2011a, b). Note that sample MK-99 is projected onto the cross-section as it was taken about 16 km to the NE of sample TSZR.

Fig. 2: (a) Representative back-scattered electron image and (b) major element chemical profile through a partially overprinted phengite. In (a), both phengite and sodic amphibole show light, relatively Fe-rich rims. The chemical profile in (b) is modified from Konrad-Schmolke et al. (2011a). (c) Si compositional map of phengites. The large grain has a pristine core and an overprinted rim of variable thickness. On the left side, overprinting has affected whole crystals and is not limited to crystal rims. Note that the increase in Si content in phengite can be attributed to fluid-induced overprinting. (d) Simplified P-T path with X_{Mg} in phengite for sample MK-52 from the EMS unit (modified from Konrad-Schmolke et al. 2011a). Peak metamorphic conditions are defined by the assemblage garnet (grt) + glaucophane (gln) + clinopyroxene (cpx) + phengite (phe) + quartz (qtz). On the retrograde path, the rock passed through the field in the center of the diagram, where paragonite (pg) became stable. Note the modeled increase in X_{Mg} during blueschist-facies overprint, which is consistent with the observed mineral chemical zoning (b).

Fig. 3: Variations of B and Li concentrations, $\delta^{11}B$ and apparent $^{40}Ar/^{39}Ar$ ages in relict phengite cores (black symbols) and overprinted rims (white symbols) from the Eclogitic Micaschists and mylonitic phengite (grey symbols) from the Tallorno Shear Zone. (a) Moderate loss of B and Li during partial overprint in phengite rims and leaching of both elements during fluid infiltration within the TSZ. Boron concentration data are from Konrad-Schmolke et al. (2011b). (b) Inversely correlated increase of $\delta^{11}B$ with decreasing B concentrations due to fluid infiltration. $\delta^{11}B$ values of cores and rims from the EMS samples are indistinguishable, indicating limited fluid influx. (c) and (d) show apparent $^{40}Ar/^{39}Ar$ ages with respect to B concentrations and $\delta^{11}B$, respectively. Dashed lines connect cores and

overprinted domains from individual samples. In all diagrams, average values with 1 SD as error bars are shown.

Fig. 4: Distribution of apparent $^{40}Ar/^{39}Ar$ ages and inverse isochron diagrams for phengites from the Eclogitic Micaschists. Vertical arrows in the inverse isochron diagrams indicate incorporation of excess ^{40}Ar. For reference, inverse isochrons with different ages relevant for the evolution of the SLZ (85, 75 and 65 Ma) were drawn, using the atmospheric $^{36}Ar/^{40}Ar$ ratio as y-axis intercept.

Fig. 5: Distribution of apparent $^{40}Ar/^{39}Ar$ ages and inverse isochron diagrams for phengites from two mylonites of the Tallorno Shear Zone. Grey diamonds mark data used in the calculations of the inverse isochrons, white diamonds are data excluded from the calculations.

Fig. 6: Overview of geochronological data obtained for the Eclogitic Micaschists. The second, blueschist-facies overprint at 65 ±3 Ma is defined based on the inverse isochron age of mylonitic mica from the shear zone. The timing of the two earlier crystallization episodes (HP crystallization and first overprint) is constrained by the inverse isochron ages of phengite cores and overprinted rims. The Lu-Hf age (Duchêne et al., 1997) was recalculated to 71.6 ±2.7 Ma using the decay constant $\lambda = 1.865 \times 10^{-11}$ year^{-1} (Scherer et al., 2001). Most of the Rb-Sr ages (Babist et al., 2006, Inger et al., 1996, and the 85 ±1 Ma age of Oberhänsli et al., 1985) are based on two- or three-point isochrons including phengite. Error bars of single spot analyses from this study are omitted for clarity.

Fig. 7: Sketch summarizing the processes relevant for $^{40}Ar/^{39}Ar$ ages, B and Li concentrations, and B isotopic compositions of the overprinted phengite rims and the recrystallizing mylonitic phengites during metasomatic overprinting. Ages are derived from the most reliable inverse isochrons. Deformation and fluid flow in the TSZ causes resetting of Ar isotopes, leaching of B and Li, and equilibration of B isotopes with an external fluid. In the EMS, B and Li are redistributed resulting in slightly decreasing rim abundances, and B isotopes equilibrate internally.

Table 1: Boron isotope analyses of phengites from the Sesia-Lanzo Zone.
Table 2: Summary of $^{40}Ar/^{39}Ar$ age data of the Sesia-Lanzo Zone samples.
Electronic Annex: Results of Ar isotopic analyses measured by UV laser ablation

Fig. 1

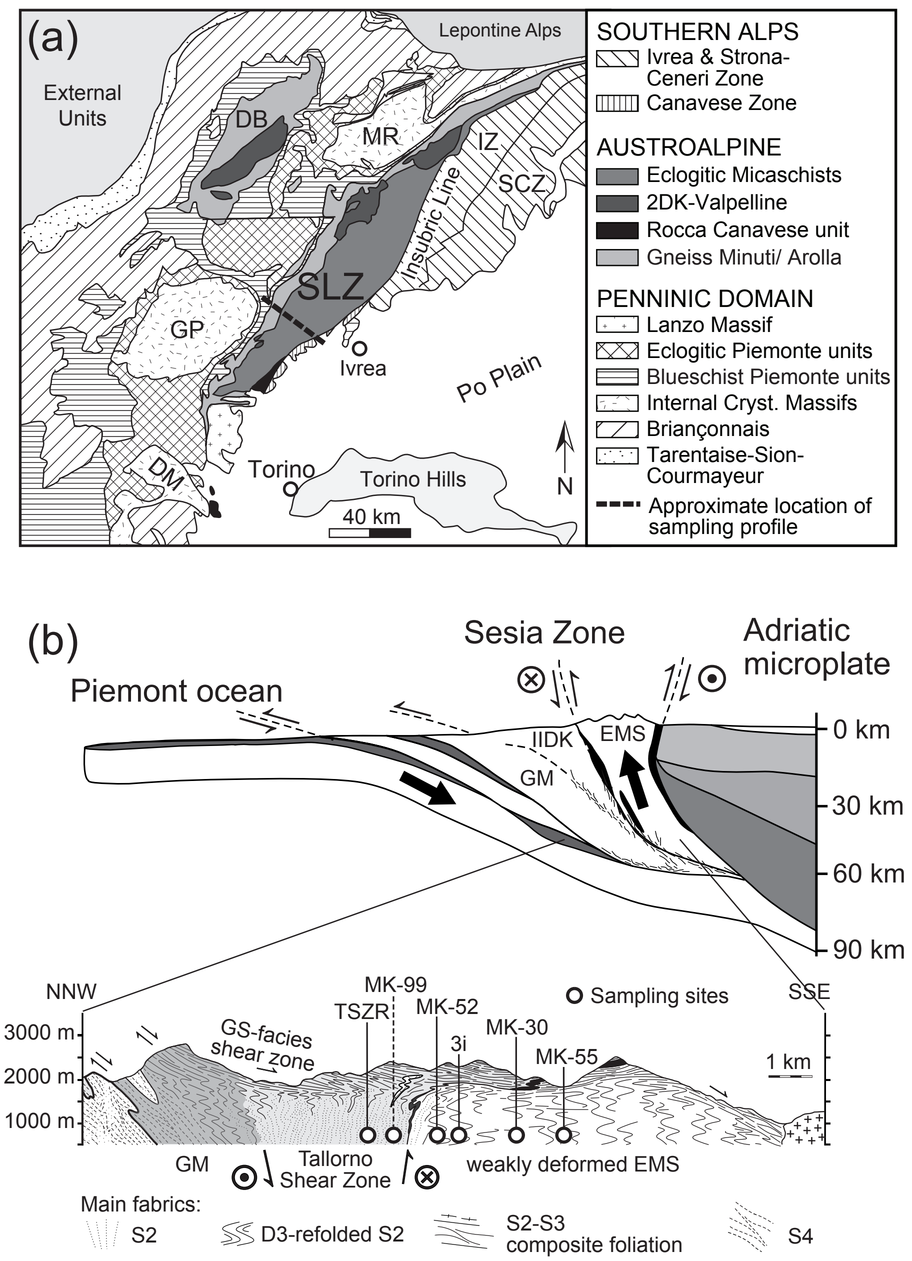
(a)
External Units
Lepontine Alps
DB
MR
IZ
SCZ
Insubric Line
SLZ
GP
Ivrea
Po Plain
DM
Torino
Torino Hills
40 km
N
SOUTHERN ALPS
Ivrea & Strona-Ceneri Zone
Canavese Zone
AUSTROALPINE
Eclogitic Micaschists
2DK-Valpelline
Rocca Canavese unit
Gneiss Minuti/ Arolla
PENNINIC DOMAIN
Lanzo Massif
Eclogitic Piemonte units
Blueschist Piemonte units
Internal Cryst. Massifs
Briançonnais
Tarentaise-Sion-Courmayeur
Approximate location of sampling profile
(b)
Sesia Zone
Adriatic microplate
Piemont ocean
IIDK
EMS
GM
0 km
30 km
60 km
90 km
NNW
SSE
MK-99
TSZR
MK-52
3i
MK-30
MK-55
Sampling sites
GS-facies shear zone
1 km
3000 m
2000 m
1000 m
GM
Tallorno Shear Zone
weakly deformed EMS
Main fabrics:
S2
D3-refolded S2
S2-S3 composite foliation
S4

Fig. 2

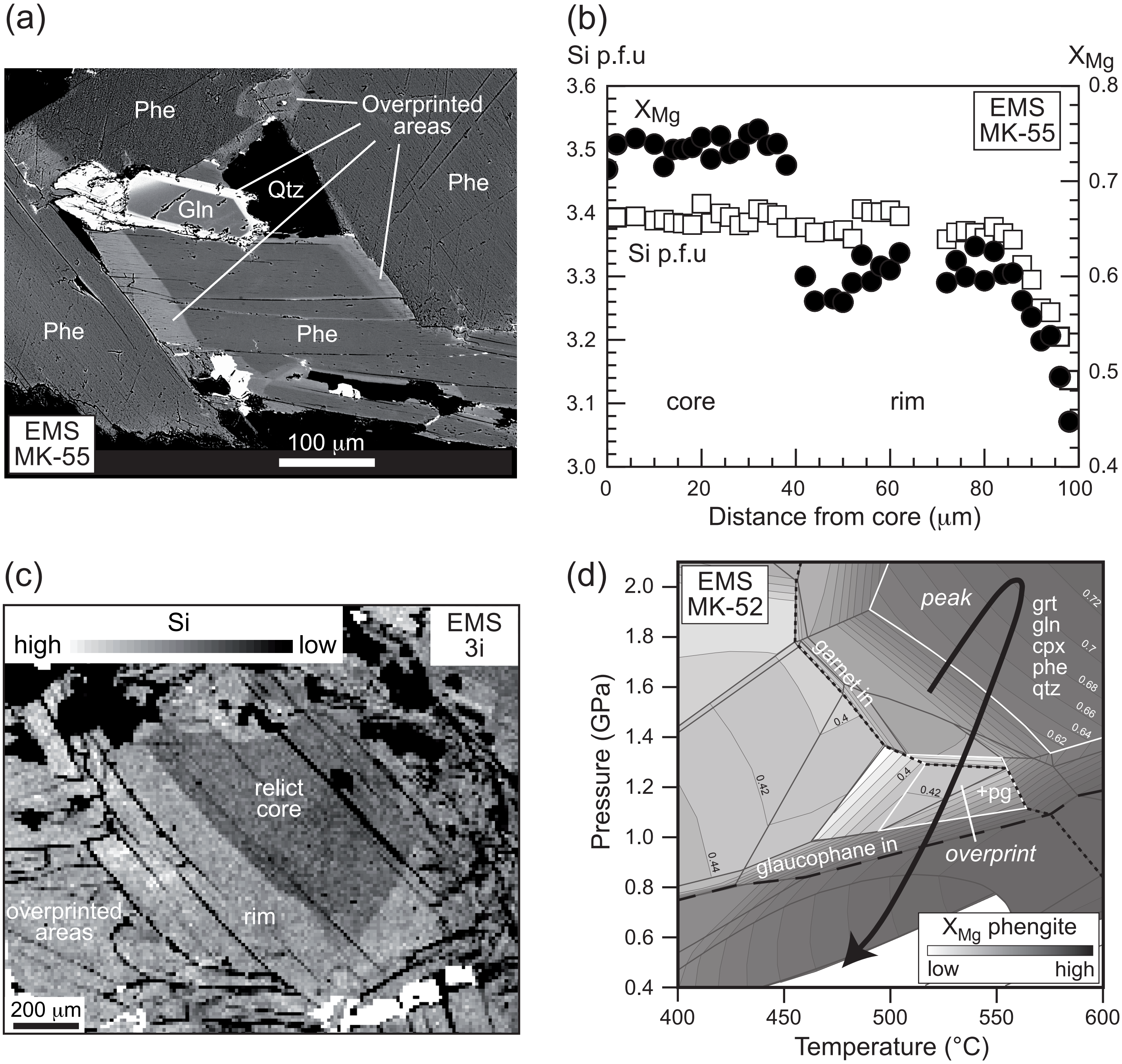

(a)
Phe
Overprinted areas
Qtz
Gln
Phe
Phe
Phe
EMS MK-55
100 μm
(b)
Si p.f.u
X$_{Mg}$
EMS MK-55
Si p.f.u
core
rim
Distance from core (μm)
(c)
Si
high
low
EMS 3i
relict core
rim
overprinted areas
200 μm
(d)
EMS MK-52
peak
grt
gln
cpx
phe
qtz
garnet in
+pg
glaucophane in
overprint
X$_{Mg}$ phengite
low
high
Pressure (GPa)
Temperature (°C)

Fig. 3

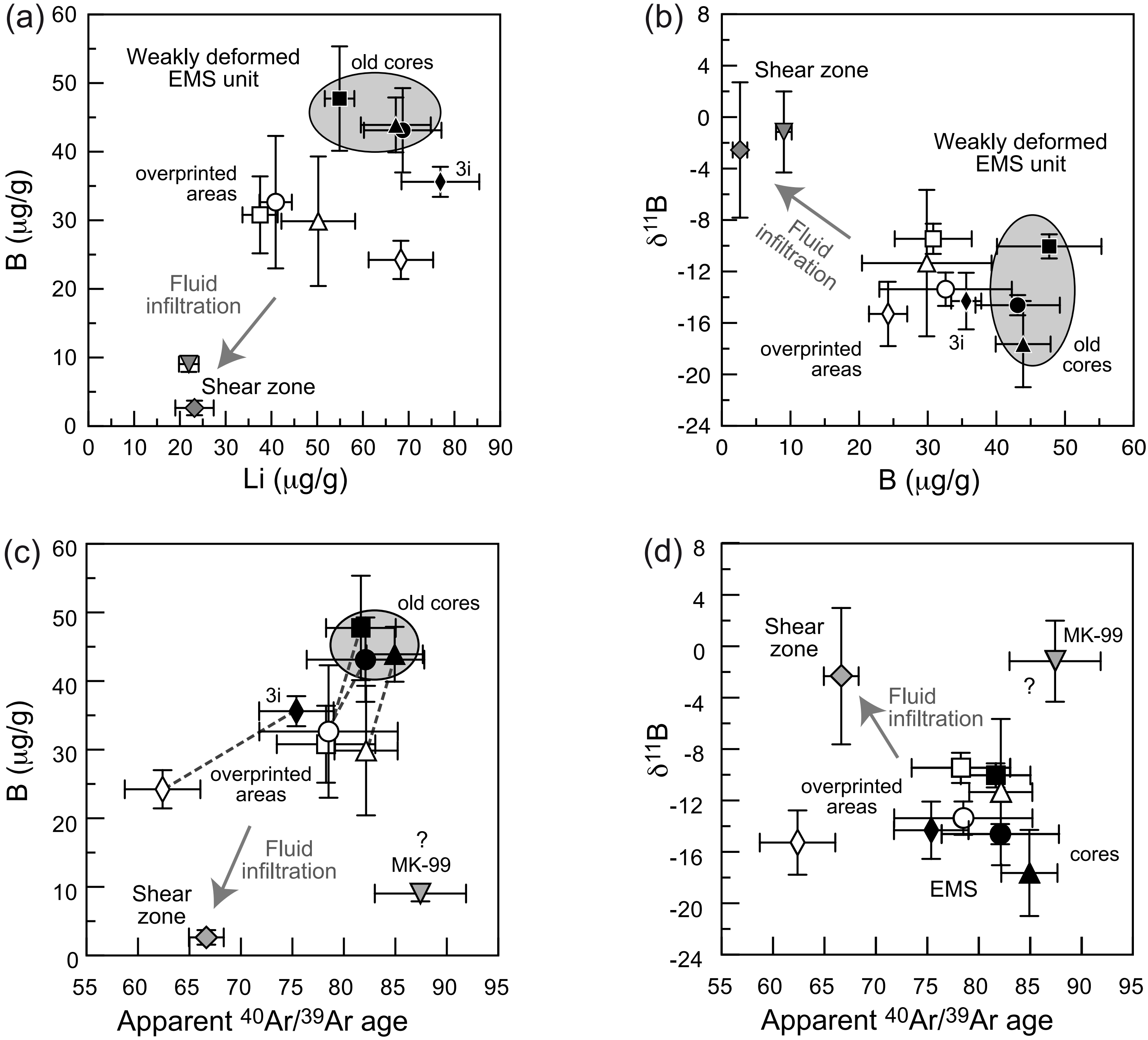

(a)
Weakly deformed EMS unit
old cores
overprinted areas
3i
Fluid infiltration
Shear zone
B (μg/g)
Li (μg/g)
(b)
Shear zone
Weakly deformed EMS unit
Fluid infiltration
overprinted areas
3i
old cores
δ11B
B (μg/g)
(c)
old cores
3i
overprinted areas
Fluid infiltration
Shear zone
?
MK-99
B (μg/g)
Apparent 40Ar/39Ar age
(d)
Shear zone
MK-99
?
Fluid infiltration
overprinted areas
cores
EMS
δ11B
Apparent 40Ar/39Ar age

Fig. 4

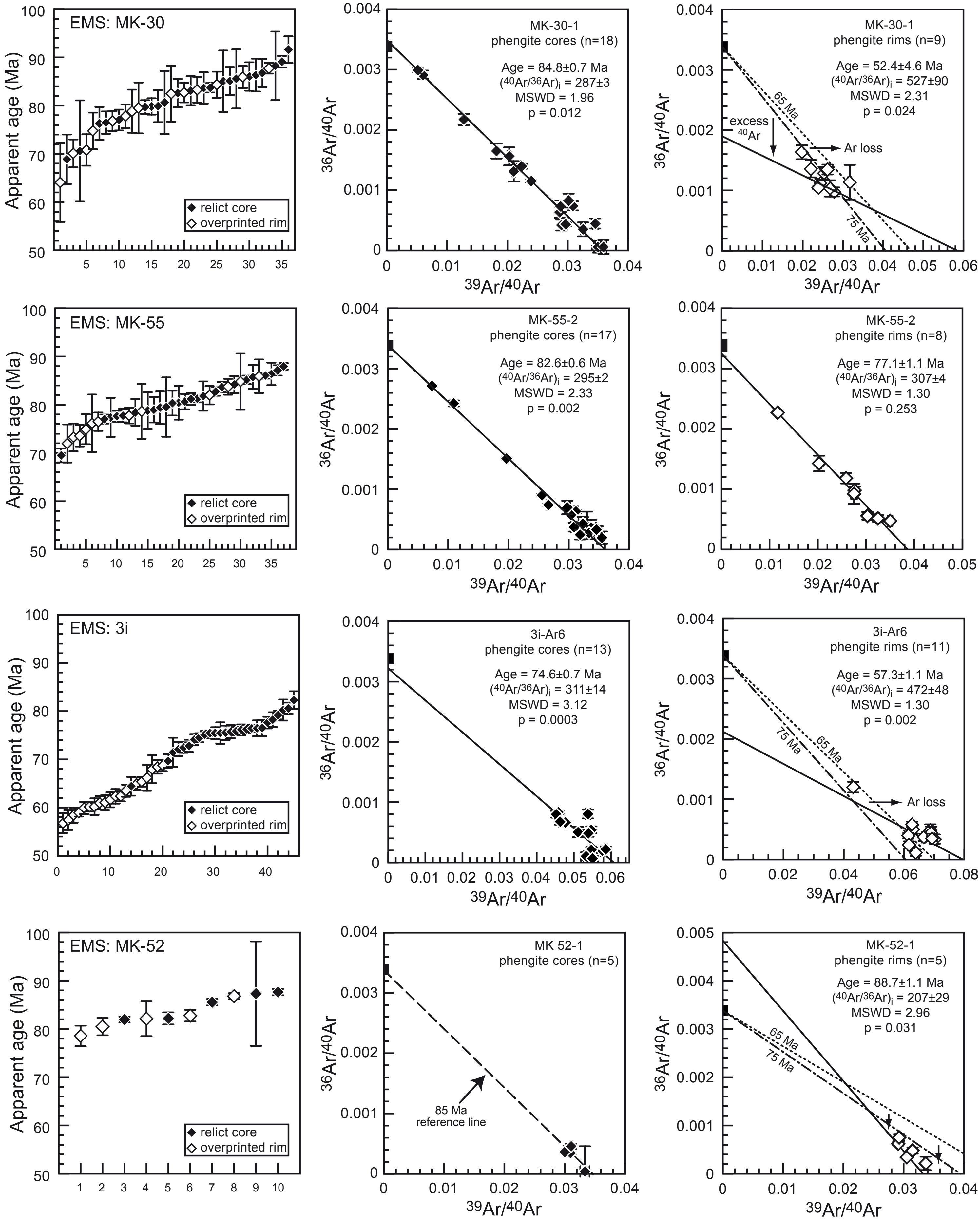

EMS: MK-30
Apparent age (Ma)
relict core
overprinted rim
MK-30-1
phengite cores (n=18)
Age = 84.8±0.7 Ma
(^{40}Ar/^{36}Ar)$_i$ = 287±3
MSWD = 1.96
p = 0.012
^{36}Ar/^{40}Ar
^{39}Ar/^{40}Ar
MK-30-1
phengite rims (n=9)
Age = 52.4±4.6 Ma
(^{40}Ar/^{36}Ar)$_i$ = 527±90
MSWD = 2.31
p = 0.024
excess ^{40}Ar
Ar loss
65 Ma
75 Ma
EMS: MK-55
MK-55-2
phengite cores (n=17)
Age = 82.6±0.6 Ma
(^{40}Ar/^{36}Ar)$_i$ = 295±2
MSWD = 2.33
p = 0.002
MK-55-2
phengite rims (n=8)
Age = 77.1±1.1 Ma
(^{40}Ar/^{36}Ar)$_i$ = 307±4
MSWD = 1.30
p = 0.253
EMS: 3i
3i-Ar6
phengite cores (n=13)
Age = 74.6±0.7 Ma
(^{40}Ar/^{36}Ar)$_i$ = 311±14
MSWD = 3.12
p = 0.0003
3i-Ar6
phengite rims (n=11)
Age = 57.3±1.1 Ma
(^{40}Ar/^{36}Ar)$_i$ = 472±48
MSWD = 1.30
p = 0.002
EMS: MK-52
MK 52-1
phengite cores (n=5)
85 Ma
reference line
MK-52-1
phengite rims (n=5)
Age = 88.7±1.1 Ma
(^{40}Ar/^{36}Ar)$_i$ = 207±29
MSWD = 2.96
p = 0.031

Fig. 5

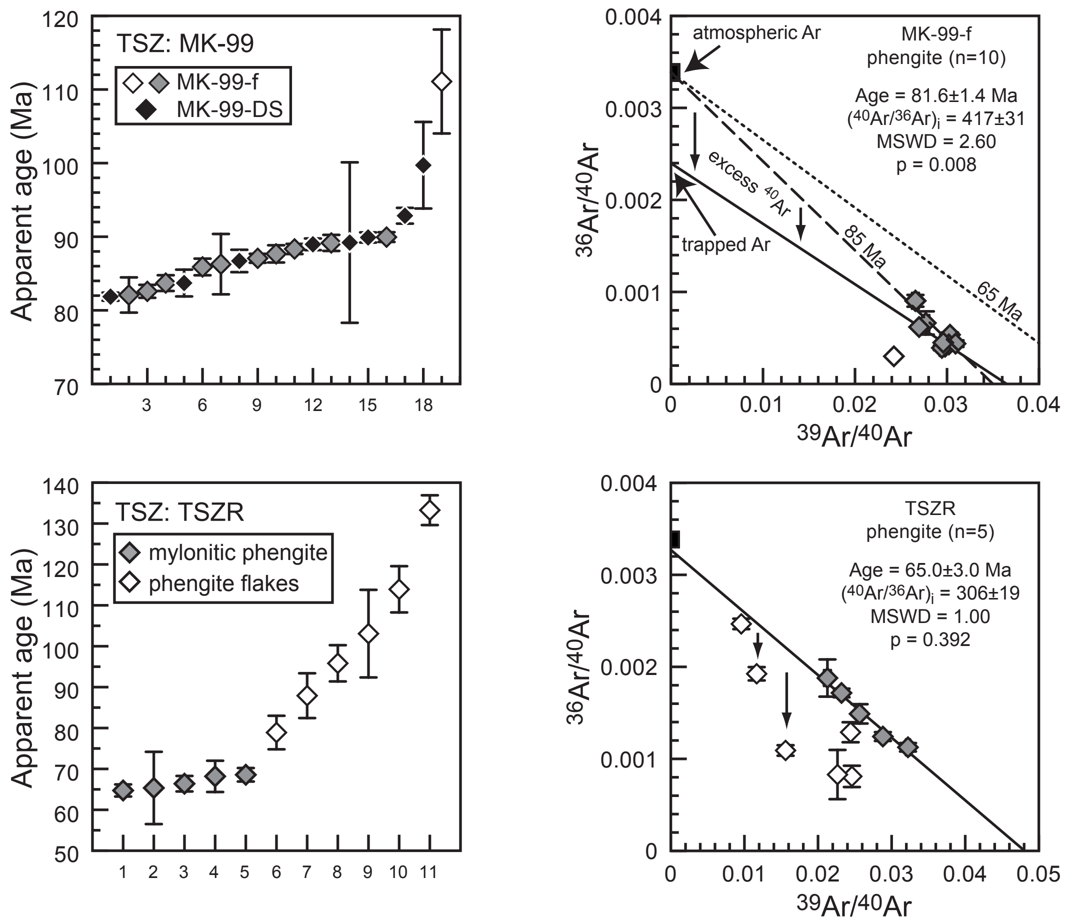
TSZ: MK-99
MK-99-f
MK-99-DS
Apparent age (Ma)
atmospheric Ar
MK-99-f
phengite (n=10)
Age = 81.6±1.4 Ma
(^{40}Ar/^{36}Ar)$_i$ = 417±31
MSWD = 2.60
p = 0.008
excess ^{40}Ar
trapped Ar
85 Ma
65 Ma
^{36}Ar/^{40}Ar
^{39}Ar/^{40}Ar
TSZ: TSZR
mylonitic phengite
phengite flakes
Apparent age (Ma)
TSZR
phengite (n=5)
Age = 65.0±3.0 Ma
(^{40}Ar/^{36}Ar)$_i$ = 306±19
MSWD = 1.00
p = 0.392
^{36}Ar/^{40}Ar
^{39}Ar/^{40}Ar

Fig. 6

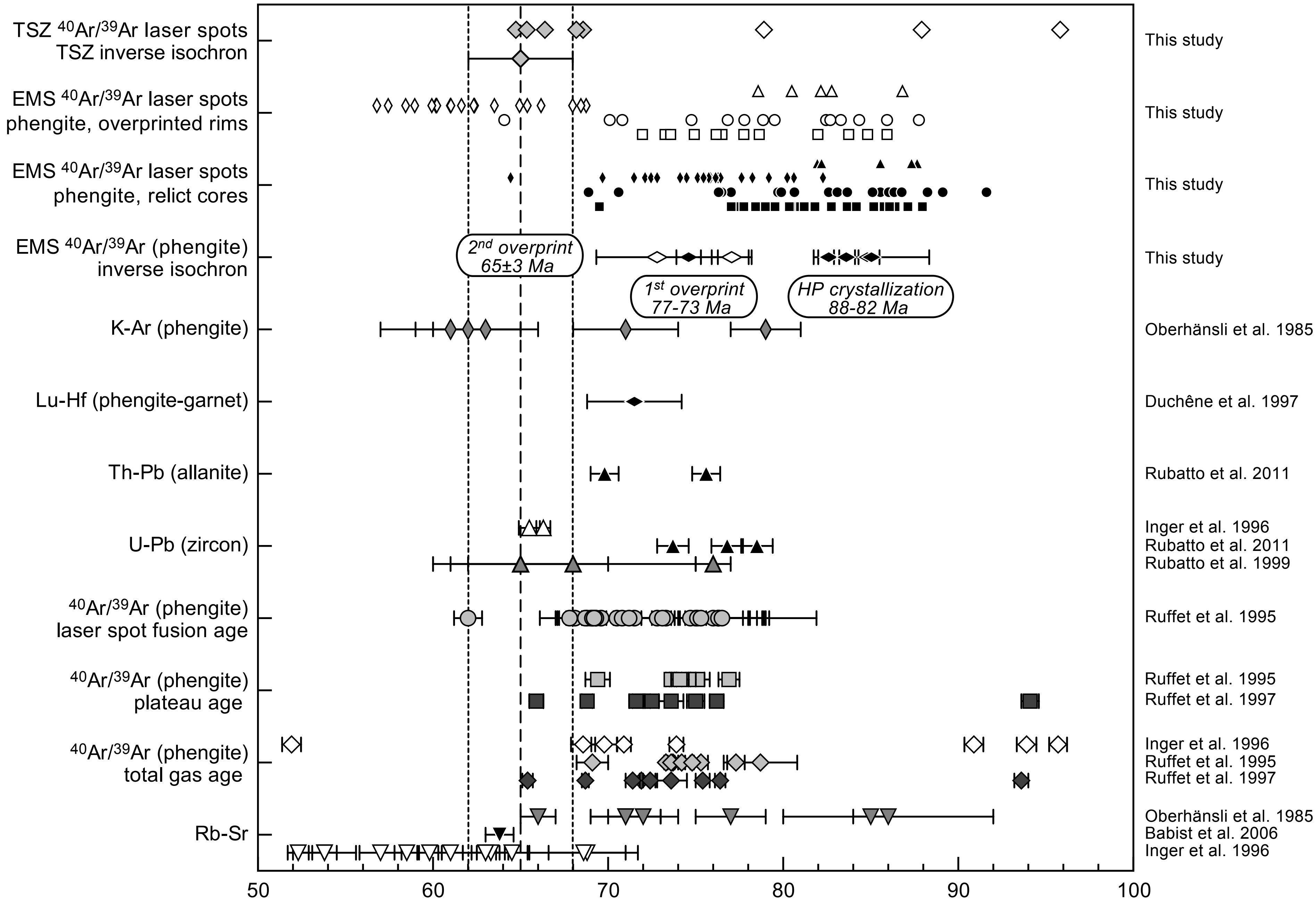

TSZ 40Ar/39Ar laser spots
TSZ inverse isochron
EMS 40Ar/39Ar laser spots
phengite, overprinted rims
EMS 40Ar/39Ar laser spots
phengite, relict cores
EMS 40Ar/39Ar (phengite)
inverse isochron
K-Ar (phengite)
Lu-Hf (phengite-garnet)
Th-Pb (allanite)
U-Pb (zircon)
40Ar/39Ar (phengite)
laser spot fusion age
40Ar/39Ar (phengite)
plateau age
40Ar/39Ar (phengite)
total gas age
Rb-Sr
2nd overprint
65±3 Ma
1st overprint
77-73 Ma
HP crystallization
88-82 Ma
50
60
70
80
90
100
This study
This study
This study
This study
Oberhänsli et al. 1985
Duchêne et al. 1997
Rubatto et al. 2011
Inger et al. 1996
Rubatto et al. 2011
Rubatto et al. 1999
Ruffet et al. 1995
Ruffet et al. 1995
Ruffet et al. 1997
Inger et al. 1996
Ruffet et al. 1995
Ruffet et al. 1997
Oberhänsli et al. 1985
Babist et al. 2006
Inger et al. 1996

Fig. 7

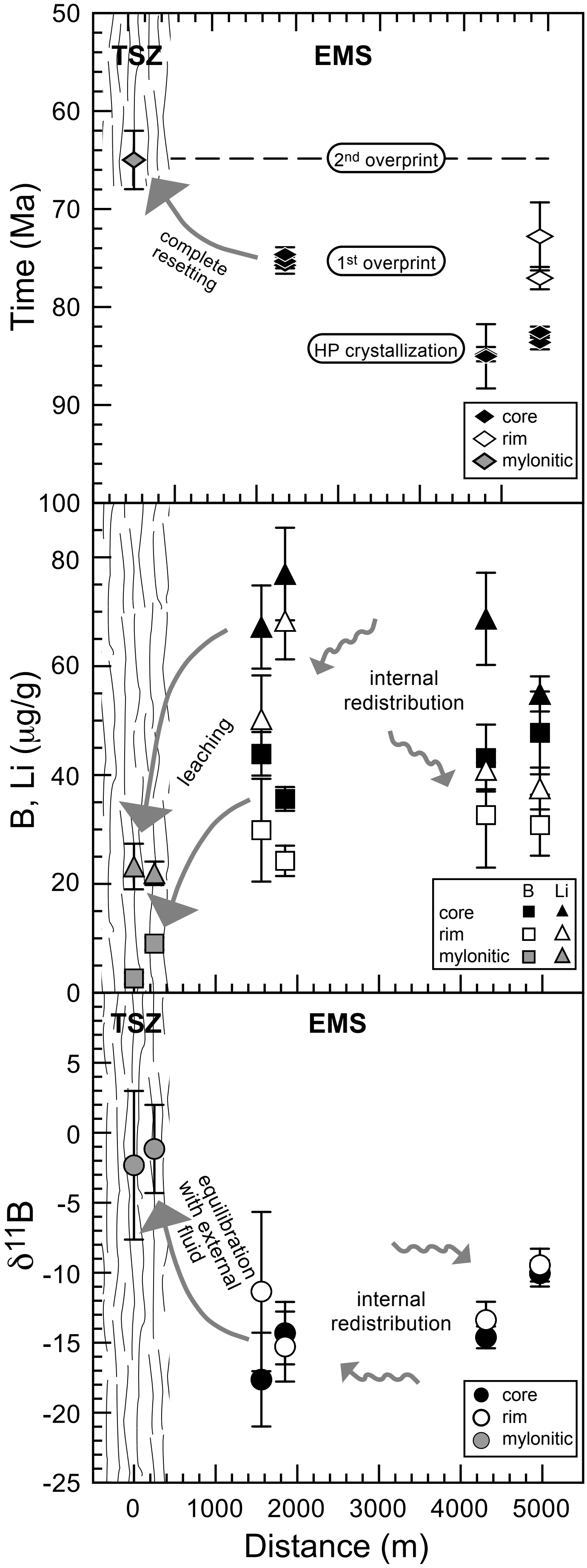

TSZ
EMS
2nd overprint
complete resetting
1st overprint
HP crystallization
core
rim
mylonitic
Time (Ma)
internal redistribution
leaching
B, Li (μg/g)
B
Li
core
rim
mylonitic
TSZ
EMS
equilibration with external fluid
internal redistribution
δ11B
core
rim
mylonitic
Distance (m)

Table 1: Boron isotope analyses of phengites

Analysis #	Position	$\delta^{11}B$	2s
MK-30, felsic gneiss*			
MK-30-11-2	core	-15.7	1.6
MK-30-11-3	core	-15.0	1.3
MK-30-11-6	core	-14.8	1.6
MK-30-11-8	core	-13.8	1.5
MK-30-11-10	core	-13.6	1.5
MK-30-11-11	core	-14.8	1.8
MK-30-11-1	rim	-13.9	1.5
MK-30-11-4	rim	-12.2	1.8
MK-30-11-5	rim	-11.3	1.8
MK-30-11-7	rim	-14.1	1.9
MK-30-11-9	rim	-13.2	1.8
MK-30-11-12	rim	-13.7	2.1
MK-30-11-13	rim	-15.2	1.8
MK-55, felsic gneiss*			
MK-55-14-1	core	-9.1	1.5
MK-55-14-3	core	-10.0	1.6
MK-55-8-1	core	-11.0	1.6
MK-55-14-2	rim	-8.3	1.8
MK-55-14-4	rim	-9.4	2.4
MK-55-8-2	rim	-10.7	1.8
MK-52, mafic gneiss*			
MK-52-1-1	core	-13.1	1.6
MK-52-1-2	core	-12.7	2.1
MK-52-4-1	core	-18.0	1.6
MK-52-4-2	core	-19.9	1.6
MK-52-6-1	core	-20.3	1.6
MK-52-6-2	core	-20.4	1.6
MK-52-6-5	core	-19.2	1.6
MK-52-1-3	rim	-9.1	2.0
MK-52-1-4	rim	-5.5	2.0
MK-52-1-5	rim	-5.5	2.1
MK-52-4-3	rim	-15.3	1.4
MK-52-6-3	rim	-19.7	1.6
MK-52-6-4	rim	-12.9	1.8
3i, micaschist‡			
30	core	-15.8	1.9
35	core	-13.5	1.1
44	core	-15.8	1.2
36	core	-15.3	1.2
39	core	-15.3	1.1
41	core	-10.1	1.5
31	rim	-14.3	1.4
37	rim	-15.6	1.2
40	rim	-11.2	1.4
32	rim	-19.0	1.0
33	rim	-13.8	1.0
34	rim	-16.9	0.9
38	rim	-16.4	1.7
MK-99, mafic mylonite*			
MK-99-1-1	core	-0.4	3.7
MK-99-1-2	core	-2.0	3.8
MK-99-1-3	core	3.6	3.8
MK-99-1-5	core	-3.1	3.6
MK-99-1-6	core	-2.8	3.6
MK-99-3-2	core	2.0	3.6
MK-99-3-4	core	-1.5	3.5
MK-99-3-5	core	-0.2	3.2
MK-99-1-4	rim	-7.1	3.4
MK-99-3-1	rim	-3.0	3.1
MK-99-3-3	rim	-3.2	3.6
MK-99-3-6	rim	3.8	3.0
TSZR, felsic mylonite‡			
18	core	-10.9	2.8
20	core	-1.0	5.5
24	core	-2.1	5.7
26	core	-7.3	3.7
19	rim	-2.6	4.0
21	rim	2.1	3.9
25	rim	6.2	5.9
27	rim	1.3	4.3
28	rim	-6.7	3.3
22	paragonite	-8.6	3.1
23	paragonite	1.3	3.1

* analyzed in Heidelberg
‡ analyzed in Potsdam

Table 2: Summary of $^{40}Ar/^{39}Ar$ age data of the Sesia-Lanzo Zone samples

Location	# of spots	Comment	Apparent spot ages AVG	±	Apparent spot ages STDEV	Apparent spot ages Wt. AVG	±	Apparent spot ages Error	Inverse isochron age	±		$(^{40}Ar/^{36}Ar)_i$	±		MSWD	χ^2	p
EMS, MK-30, felsic gneiss																	
MK-30-1 cores	18	all	81.9	±	6.1	83.6	±	0.5	84.8	±	0.7	287	±	3	1.96	31.36	0.012
MK-30-2 cores	4	all	83.2	±	3.9	81.6	±	1.1	85.0	±	3.3	243	±	57	1.86	3.72	0.156
MK-30-1 rims	9	all	77.6	±	7.2	83.3	±	0.8	52.4	±	4.6	527	±	90	2.31	16.17	0.024
MK-30-2 rims	5	all	80.1	±	6.2	80.9	±	1.1	80.2	±	2.2	308	±	43	2.64	7.92	0.048
EMS, MK-55, felsic gneiss																	
MK-55-1 cores	7	all	82.8	±	3.7	84.0	±	0.4	83.6	±	0.7	314	±	13	4.70	23.50	0.000
MK-55-2 cores	17	1 excluded	81.2	±	3.3	82.3	±	0.4	82.6	±	0.6	295	±	2	2.33	35.02	0.002
MK-55-1 rims	4	all	76.9	±	6.3	76.2	±	1.6	72.8	±	3.5	388	±	118	2.22	4.44	0.109
MK-55-2 rims	8	all	79.0	±	4.2	79.3	±	0.8	77.1	±	1.1	307	±	4	1.30	7.80	0.253
EMS, MK-52, mafic gneiss																	
cores	5	all	84.9	±	2.7	84.6	±	0.3	–		–	–		–	–	–	–
rims	5	all	82.2	±	3.1	85.0	±	0.5	88.7	±	1.1	207	±	29	2.96	8.88	0.031
EMS, 3i, micaschist																	
3i-Ar-4-05 cores	5	all	76.0	±	3.1	75.9	±	0.5	75.8	±	0.9	299	±	15	1.60	4.80	0.187
3i-Ar-4-10 cores	8	all	75.7	±	1.7	75.9	±	0.4	75.3	±	0.7	412	±	85	1.81	10.88	0.092
3i-Ar-6-06 cores	13	all	74.9	±	4.7	75.2	±	0.4	74.6	±	0.7	311	±	14	3.12	34.31	0.000
3i-Ar-4-10 rims	8	all	62.6	±	2.2	62.4	±	0.5	60.2	±	1.4	442	±	102	1.23	7.41	0.285
3i-Ar-6-06 rims	11	all	61.7	±	4.4	62.0	±	0.4	57.3	±	1.1	472	±	48	2.95	26.59	0.002
TSZ, MK-99, mafic mylonite																	
MK-99-f mylonitic	10	1 excluded	86.3	±	2.7	87.2	±	0.3	81.6	±	1.4	417	±	31	2.60	20.80	0.008
MK-99-DS mylonitic	8	all	89.1	±	5.5	86.6	±	0.3	62.3	±	2.6	954	±	114	2.80	16.80	0.010
TSZ, TSZR, felsic mylonite																	
mylonitic phengite	5	selection 1	66.6	±	1.7	66.5	±	0.9	65.0	±	3.0	306	±	19	1.00	3.00	0.392
phengite flakes	6	selection 2	102.2	±	19.5	104.3	±	2.0	100.2	±	3.0	315	±	10	5.44	21.76	0.000

Electronic Annex 1: Results of *in situ* argon isotopic analyses measured by UV laser ablation

Analysis ID	Laser output (mJ)	$^{40}Ar/^{39}Ar$	$^{37}Ar/^{39}Ar$	$^{36}Ar/^{39}Ar$ ($\times 10^{-3}$)	K/Ca	$^{40}Ar^*$ (%)	$^{40}Ar^*/^{39}Ar_K$	Age (Ma) ± 1s (Ma)
MK-30 - cores	**MK-30-1, d10**	**J=0.001723**						
U0701402	0.8	78.28 ± 0.82	0.013 ± 0.118	170.11 ± 7.41	45.4	35.8	28.02 ± 2.15	85.06 ± 6.37
U0701403	0.8	54.98 ± 0.42	0.083 ± 0.160	90.72 ± 6.97	7.1	51.3	28.19 ± 2.06	85.55 ± 6.13
U0701404	0.8	49.26 ± 0.60	0.019 ± 0.056	76.93 ± 7.36	30.5	53.9	26.53 ± 2.19	80.64 ± 6.53
U0701405	0.8	47.51 ± 0.60	0.019 ± 0.061	62.32 ± 8.04	31.2	61.2	29.09 ± 2.40	88.24 ± 7.11
U0701407	0.8	34.53 ± 0.18	0.007 ± 0.039	14.54 ± 3.10	84.0	87.6	30.23 ± 0.93	91.61 ± 2.77
U0701411	0.8	166.48 ± 1.17	1.223 ± 0.199	485.64 ± 12.28	0.5	13.9	23.16 ± 3.51	70.60 ± 10.48
U0701414	0.8	32.40 ± 0.09	0.009 ± 0.066	23.98 ± 2.42	64.2	78.1	25.31 ± 0.72	77.02 ± 2.16
U0701416	0.8	34.86 ± 0.23	0.004 ± 0.016	22.03 ± 3.27	151.1	81.3	28.35 ± 0.99	86.03 ± 2.94
U0701418	0.8	34.70 ± 0.15	0.009 ± 0.013	25.43 ± 3.28	65.3	78.4	27.19 ± 0.98	82.60 ± 2.92
MK-30 - cores	**MK-30-1, d10**	**J=0.001723**						
U0800201	0.5	41.74 ± 0.20	0.207 ± 0.12	48.10 ± 0.95	2.8	66.0	27.56 ± 0.31	83.70 ± 0.97
U0800202	0.5	44.67 ± 0.32	0.274 ± 0.27	62.47 ± 1.82	2.1	58.8	26.26 ± 0.56	79.82 ± 1.70
U0800203	0.5	33.71 ± 0.25	0.041 ± 0.37	14.64 ± 1.08	14.2	87.2	29.39 ± 0.39	89.11 ± 1.20
U0800204	0.5	194.49 ± 1.97	0.423 ± 0.87	581.95 ± 8.06	1.4	11.6	22.59 ± 1.71	68.88 ± 5.13
U0800205	0.5	28.52 ± 0.55	0.810 ± 0.33	2.08 ± 2.71	0.7	98.2	28.03 ± 0.97	85.10 ± 2.89
U0800206	0.5	27.80 ± 0.39	1.104 ± 0.83	2.09 ± 3.13	0.5	98.3	27.36 ± 1.01	83.09 ± 3.02
U0800207	0.5	28.91 ± 0.39	1.005 ± 0.46	13.31 ± 2.33	0.6	86.8	25.13 ± 0.77	76.48 ± 2.32
U0800208	0.5	33.18 ± 0.20	0.040 ± 1.04	27.45 ± 3.80	14.8	75.6	25.08 ± 1.14	76.31 ± 3.42
U0800209	0.5	30.71 ± 0.33	0.487 ± 1.16	10.97 ± 3.51	1.2	89.7	27.55 ± 1.09	83.66 ± 3.26
MK-30 - rims	**MK-30-1, d10**	**J=0.001723**						
U0701401	0.8	50.54 ± 0.49	0.075 ± 0.090	82.57 ± 5.94	7.9	51.7	26.15 ± 1.77	79.51 ± 5.26
U0701406	0.8	40.99 ± 0.25	0.065 ± 0.110	45.94 ± 2.98	9.1	66.9	27.42 ± 0.89	83.29 ± 2.67
U0701408	0.8	45.36 ± 0.46	0.054 ± 0.213	61.68 ± 6.54	10.9	59.8	27.14 ± 1.95	82.45 ± 5.79
U0701409	0.8	31.55 ± 0.42	0.024 ± 0.157	35.77 ± 9.15	24.9	66.5	20.98 ± 2.72	64.07 ± 8.17
U0701410	0.8	41.83 ± 0.11	0.029 ± 0.025	43.66 ± 1.16	20.5	69.2	28.93 ± 0.35	87.75 ± 1.10
U0701412	0.8	39.51 ± 0.26	0.273 ± 0.128	50.75 ± 4.26	2.2	62.1	24.56 ± 1.27	74.76 ± 3.80
U0701413	0.8	38.17 ± 0.40	0.071 ± 0.066	51.40 ± 3.18	8.3	60.2	22.99 ± 0.96	70.09 ± 2.88
U0701415	0.8	35.92 ± 0.26	0.029 ± 0.081	35.03 ± 2.70	20.1	71.2	25.57 ± 0.82	77.78 ± 2.46
U0701417	0.8	37.31 ± 0.25	0.134 ± 0.110	38.57 ± 5.04	4.4	69.5	25.93 ± 1.50	78.85 ± 4.47
MK-30 - cores	**MK-30-2-4, d14**	**J=0.001703**						
U0701503	0.8	34.52 ± 0.18	0.132 ± 0.065	27.14 ± 1.51	4.5	76.8	26.52 ± 0.47	79.70 ± 1.42
U0701508	0.8	35.18 ± 0.29	0.008 ± 0.072	21.64 ± 3.73	75.1	81.8	28.78 ± 1.13	86.34 ± 3.34
U0701509	0.8	32.11 ± 0.31	0.022 ± 0.068	10.77 ± 3.12	27.0	90.1	28.93 ± 0.97	86.77 ± 2.86
U0701510	0.8	31.10 ± 0.19	0.001 ± 0.095	15.29 ± 3.71	415.3	85.5	26.59 ± 1.11	79.89 ± 3.27
MK-30 - rims	**MK-30-2-4, d14**	**J=0.001703**						
U0701501	0.8	35.97 ± 0.13	0.069 ± 0.024	35.31 ± 2.33	8.5	71.0	25.55 ± 0.69	76.83 ± 2.07
U0701504	0.8	33.91 ± 0.21	0.009 ± 0.097	19.67 ± 3.04	63.3	82.9	28.10 ± 0.92	84.34 ± 2.71
U0701505	0.8	27.04 ± 0.18	0.019 ± 0.085	11.96 ± 3.67	31.1	86.9	23.51 ± 1.10	70.81 ± 3.25
U0701506	0.8	31.34 ± 0.13	0.016 ± 0.078	9.11 ± 2.57	37.7	91.4	28.65 ± 0.77	85.93 ± 2.28
U0701507	0.8	31.59 ± 0.24	0.005 ± 0.044	13.70 ± 2.18	113.9	87.2	27.54 ± 0.68	82.69 ± 2.03
MK-55 - cores	**MK-55-2, d16**	**J=0.001687**						
U0800101	0.8	39.07 ± 0.20	0.072 ± 0.078	35.26 ± 0.77	8.2	73.3	28.66 ± 0.28	85.17 ± 0.89
U0800102	0.8	37.54 ± 0.30	0.103 ± 0.162	27.86 ± 0.77	5.7	78.1	29.33 ± 0.34	87.12 ± 1.06
U0800103	0.8	74.26 ± 0.62	0.440 ± 0.228	172.74 ± 1.90	1.3	31.3	23.28 ± 0.49	69.50 ± 1.45
U0800104	0.8	136.73 ± 0.39	0.122 ± 0.148	371.07 ± 1.86	4.8	19.8	27.10 ± 0.54	80.65 ± 1.60
U0800105	0.8	32.04 ± 0.31	0.078 ± 0.317	20.28 ± 0.87	7.5	81.3	26.06 ± 0.38	77.63 ± 1.14
U0800106	0.8	50.75 ± 0.33	0.072 ± 0.137	76.60 ± 1.03	8.2	55.4	28.13 ± 0.35	83.65 ± 1.07
U0800107	0.8	32.91 ± 0.24	0.096 ± 0.161	19.01 ± 0.40	6.1	83.0	27.31 ± 0.24	81.26 ± 0.77
U0800110	0.5	33.52 ± 0.48	2.321 ± 1.276	24.39 ± 3.70	0.3	79.4	26.68 ± 1.17	79.42 ± 3.42
U0800111	0.5	30.18 ± 0.49	3.770 ± 1.787	13.70 ± 6.91	0.2	88.2	26.71 ± 2.11	79.53 ± 6.15
U0800112	0.5	29.62 ± 0.66	0.552 ± 0.809	10.98 ± 3.92	1.1	89.3	26.46 ± 1.31	78.79 ± 3.82
U0800113	0.5	30.89 ± 0.70	0.543 ± 0.867	13.38 ± 3.47	1.1	87.4	27.02 ± 1.20	80.43 ± 3.51
U0800114	0.5	91.40 ± 1.19	0.603 ± 1.238	221.71 ± 5.29	1.0	28.4	25.98 ± 1.39	77.39 ± 4.05
U0800115	0.5	29.95 ± 0.41	0.087 ± 0.999	8.36 ± 3.23	6.7	91.8	27.50 ± 1.04	81.81 ± 3.03
U0800116	0.5	28.72 ± 0.40	0.454 ± 1.334	8.32 ± 2.89	1.3	91.6	26.34 ± 0.95	78.42 ± 2.77
U0800117	0.5	28.16 ± 0.31	0.200 ± 1.300	5.62 ± 2.84	2.9	94.2	26.53 ± 0.91	78.98 ± 2.66
U0800122	0.5	28.91 ± 0.22	0.217 ± 0.450	9.61 ± 1.41	2.7	90.3	26.10 ± 0.47	77.75 ± 1.40
U0800125	0.5	32.39 ± 0.52	1.061 ± 1.013	12.50 ± 2.33	0.6	89.0	28.86 ± 0.84	85.76 ± 2.47
U0800126	0.5	31.36 ± 0.26	0.336 ± 1.358	7.92 ± 2.47	1.8	92.7	29.08 ± 0.79	86.39 ± 2.33
MK-55 - rims	**MK-55-2, d16**	**J=0.001687**						
U0800108	0.8	85.47 ± 0.30	0.318 ± 0.318	194.09 ± 1.85	1.9	32.9	28.16 ± 0.56	83.74 ± 1.65
U0800109	0.8	28.54 ± 0.39	0.951 ± 0.433	13.96 ± 3.04	0.6	86.0	24.56 ± 0.96	73.25 ± 2.83
U0800118	0.5	38.64 ± 0.38	0.418 ± 0.966	45.93 ± 3.38	1.4	65.0	25.14 ± 1.04	74.92 ± 3.06
U0800119	0.5	33.00 ± 0.19	0.103 ± 0.731	18.47 ± 2.08	5.7	83.5	27.56 ± 0.64	81.98 ± 1.90
U0800120	0.5	49.32 ± 0.91	0.485 ± 2.562	70.61 ± 6.39	1.2	57.8	28.54 ± 1.97	84.82 ± 5.72
U0800121	0.5	36.17 ± 0.17	0.770 ± 0.679	35.91 ± 2.10	0.8	70.9	25.67 ± 0.64	76.50 ± 1.89
U0800123	0.5	30.78 ± 0.29	0.770 ± 0.496	16.22 ± 1.63	0.8	84.8	26.11 ± 0.55	77.75 ± 1.63
U0800127	0.5	36.29 ± 0.77	1.085 ± 1.717	34.03 ± 6.14	0.5	72.7	26.41 ± 1.91	78.63 ± 5.57
MK-55 - cores	**MK-55-1, d10**	**J=0.001723**						
U0701902	0.8	31.83 ± 0.05	0.021 ± 0.019	11.77 ± 0.69	27.4	89.1	28.36 ± 0.21	86.07 ± 0.70
U0701904	0.8	30.86 ± 0.14	0.002 ± 0.022	6.33 ± 0.61	359.0	93.9	28.99 ± 0.22	87.95 ± 0.75
U0701905	0.8	30.75 ± 0.20	0.006 ± 0.072	10.24 ± 1.87	92.9	90.2	27.72 ± 0.58	84.18 ± 1.76
U0701906	0.8	28.68 ± 0.16	0.004 ± 0.041	6.62 ± 1.29	144.4	93.2	26.72 ± 0.41	81.20 ± 1.26
U0701908	0.8	27.93 ± 0.31	0.008 ± 0.042	5.06 ± 2.69	70.7	94.6	26.43 ± 0.85	80.35 ± 2.54
U0701910	0.8	27.99 ± 0.13	0.035 ± 0.020	9.04 ± 0.96	16.6	90.5	25.32 ± 0.31	77.03 ± 0.96
U0701912	0.8	37.49 ± 0.18	0.003 ± 0.024	34.68 ± 0.87	201.6	72.7	27.24 ± 0.29	82.75 ± 0.91
MK-55 - rims	**MK-55-1, d10**	**J=0.001723**						
U0701909	0.8	29.79 ± 0.20	0.061 ± 0.044	5.01 ± 3.82	9.7	95.1	28.31 ± 1.14	85.93 ± 3.41
U0701911	0.8	27.00 ± 0.24	0.083 ± 0.127	6.72 ± 6.58	7.1	92.7	25.03 ± 1.96	76.17 ± 5.84
U0701913	0.8	23.90 ± 0.18	0.026 ± 0.091	0.97 ± 4.35	22.6	98.8	23.62 ± 1.30	71.96 ± 3.89
U0701914	0.8	29.97 ± 0.22	0.070 ± 0.073	19.69 ± 2.40	8.4	80.6	24.16 ± 0.73	73.57 ± 2.20
3i - cores	**3i-Ar6**	**J=0.002567**						
U1300602	0.7	18.57 ± 0.21	0.29 ± 1.03	15.01 ± 1.31	2.0	76.2	14.16 ± 0.43	64.43 ± 1.93
U1300603	0.7	18.27 ± 0.11	0.21 ± 1.11	9.97 ± 0.97	2.8	84.0	15.34 ± 0.32	69.68 ± 1.43
U1300605	0.7	21.80 ± 0.11	0.16 ± 0.71	18.25 ± 0.60	3.6	75.3	16.42 ± 0.20	74.48 ± 0.96
U1300607	0.7	19.54 ± 0.08	0.21 ± 1.24	9.90 ± 1.60	2.8	85.1	16.64 ± 0.49	75.46 ± 2.19
U1300609	0.7	22.09 ± 0.06	0.54 ± 1.01	17.81 ± 1.20	1.1	76.4	16.87 ± 0.37	76.50 ± 1.66
U1300611	0.7	17.34 ± 0.13	0.18 ± 1.11	3.45 ± 0.65	3.3	94.2	16.34 ± 0.25	74.11 ± 1.14
U1300613	0.7	18.26 ± 0.12	0.21 ± 1.12	3.90 ± 0.76	2.8	93.8	17.13 ± 0.27	77.62 ± 1.22
U1300615	0.7	20.93 ± 0.14	0.13 ± 0.92	13.94 ± 0.39	4.5	80.4	16.83 ± 0.18	76.28 ± 0.85
U1300616	0.7	18.53 ± 0.09	0.42 ± 1.14	9.08 ± 0.99	1.4	85.7	15.89 ± 0.32	72.11 ± 1.45
U1300617	0.7	17.05 ± 0.08	1.37 ± 0.63	4.10 ± 0.74	0.4	93.5	15.96 ± 0.24	72.45 ± 1.10
U1300619	0.7	18.72 ± 0.21	2.81 ± 1.00	2.75 ± 1.15	0.2	96.9	18.18 ± 0.41	82.27 ± 1.83
U1300622	0.7	18.14 ± 0.12	1.12 ± 0.61	1.51 ± 0.77	0.5	98.1	17.80 ± 0.26	80.61 ± 1.19
U1300624	0.7	21.57 ± 0.13	0.22 ± 0.92	14.65 ± 1.05	2.7	80.0	17.27 ± 0.34	78.24 ± 1.52
3i - rims	**3i-Ar6**	**J=0.002567**						
U1300601	0.7	23.17 ± 0.31	0.46 ± 2.91	27.92 ± 1.90	1.3	64.5	14.96 ± 0.64	67.97 ± 2.87
U1300604	0.7	15.88 ± 0.13	0.31 ± 1.59	8.04 ± 1.01	1.9	85.2	13.54 ± 0.35	61.62 ± 1.57
U1300606	0.7	15.96 ± 0.04	0.15 ± 0.59	9.36 ± 0.69	3.8	82.8	13.21 ± 0.21	60.16 ± 0.97
U1300608	0.7	16.28 ± 0.11	0.43 ± 1.20	6.56 ± 0.60	1.4	88.3	14.38 ± 0.23	65.38 ± 1.04
U1300610	0.7	14.53 ± 0.18	1.16 ± 1.84	7.39 ± 1.32	0.5	85.6	12.46 ± 0.45	56.79 ± 2.02
U1300612	0.7	14.49 ± 0.09	0.28 ± 1.66	6.46 ± 1.43	2.1	87.0	12.60 ± 0.45	57.44 ± 2.04
U1300614	0.7	14.25 ± 0.11	0.21 ± 1.22	4.89 ± 1.05	2.8	90.0	12.82 ± 0.34	58.43 ± 1.55
U1300618	0.7	15.02 ± 0.14	0.21 ± 0.63	5.57 ± 0.91	2.8	89.2	13.39 ± 0.30	60.99 ± 1.37
U1300620	0.7	15.63 ± 0.09	2.48 ± 1.21	2.46 ± 0.75	0.2	96.7	15.13 ± 0.26	68.74 ± 1.19
U1300621	0.7	14.42 ± 0.06	0.54 ± 0.85	5.19 ± 0.51	1.1	89.7	12.94 ± 0.18	58.95 ± 0.82
U1300623	0.7	16.22 ± 0.11	0.47 ± 0.90	4.05 ± 0.94	1.3	92.9	15.06 ± 0.31	68.44 ± 1.39
3i - cores	**3i-Ar4**	**J=0.002568**						
U1300501	0.95	29.20 ± 0.28	0.09 ± 0.28	45.59 ± 2.18	6.9	53.9	15.74 ± 0.66	71.48 ± 2.97
U1300502	0.95	22.39 ± 0.15	0.11 ± 0.38	15.89 ± 1.57	5.5	79.1	17.71 ± 0.48	80.23 ± 2.16
U1300503	0.95	19.59 ± 0.10	0.09 ± 0.38	9.28 ± 1.19	6.5	86.0	16.86 ± 0.36	76.45 ± 1.63
U1300509	0.95	21.20 ± 0.05	0.02 ± 0.09	14.73 ± 0.55	37.5	79.5	16.85 ± 0.17	76.42 ± 0.81
U1300510	0.95	18.54 ± 0.06	0.07 ± 0.07	6.49 ± 0.36	8.0	89.7	16.63 ± 0.12	75.44 ± 0.60
U1301004	0.7	16.72 ± 0.08	0.13 ± 0.59	0.61 ± 0.46	4.7	99.0	16.55 ± 0.17	75.11 ± 0.79
U1301005	0.7	16.15 ± 0.19	0.90 ± 0.81	0.67 ± 0.66	0.7	99.2	16.03 ± 0.28	72.80 ± 1.29
U1301006	0.7	17.50 ± 0.05	0.94 ± 0.57	2.94 ± 0.60	0.6	95.5	16.72 ± 0.19	75.85 ± 0.90
U1301010	0.7	17.17 ± 0.16	1.67 ± 0.78	2.29 ± 0.95	0.4	96.9	16.65 ± 0.33	75.52 ± 1.48
U1301011	0.7	17.49 ± 0.11	2.41 ± 1.41	3.44 ± 0.85	0.2	95.3	16.70 ± 0.30	75.75 ± 1.36
U1301012	0.7	17.46 ± 0.13	1.74 ± 0.88	0.52 ± 0.43	0.3	99.9	17.47 ± 0.20	79.18 ± 0.93
U1301013	0.7	17.98 ± 0.16	0.22 ± 0.78	4.63 ± 0.72	2.7	92.5	16.63 ± 0.27	75.45 ± 1.22
U1301014	0.7	16.86 ± 0.15	0.19 ± 0.98	0.32 ± 0.59	3.0	99.5	16.79 ± 0.24	76.14 ± 1.12
3i - rims	**3i-Ar4**	**J=0.002568**						
U1301001	0.7	14.48 ± 0.08	0.26 ± 1.15	3.76 ± 1.05	2.3	92.5	13.40 ± 0.34	61.02 ± 1.52
U1301002	0.7	14.10 ± 0.09	0.17 ± 1.02	1.43 ± 0.67	3.4	97.1	13.70 ± 0.23	62.37 ± 1.07
U1301003	0.7	16.02 ± 0.07	0.20 ± 0.90	7.05 ± 0.87	3.0	87.1	13.95 ± 0.28	63.50 ± 1.26
U1301007	0.7	15.51 ± 0.14	1.69 ± 2.56	3.77 ± 1.80	0.3	93.7	14.55 ± 0.59	66.17 ± 2.64
U1301008	0.7	13.83 ± 0.06	1.16 ± 1.59	2.45 ± 1.18	0.5	95.5	13.22 ± 0.38	60.21 ± 1.71
U1301009	0.7	14.19 ± 0.16	1.19 ± 1.43	3.88 ± 0.68	0.5	92.6	13.15 ± 0.28	59.93 ± 1.26
U1301015	0.7	14.67 ± 0.10	0.26 ± 1.67	3.39 ± 0.96	2.3	93.3	13.69 ± 0.33	62.33 ± 1.50
U1301016	0.7	14.76 ± 0.07	0.27 ± 1.36	1.72 ± 0.86	2.2	96.7	14.27 ± 0.29	64.94 ± 1.30
MK-52 - cores	**MK-52-1, d17**	**J=0.001674**						
U0702201	0.8	32.20 ± 0.04	0.002 ± 0.015	15.03 ± 0.54	282.1	86.2	27.76 ± 0.16	81.95 ± 0.57
U0702203	0.8	32.29 ± 0.12	0.003 ± 0.016	11.10 ± 0.56	208.1	89.8	29.01 ± 0.20	85.55 ± 0.66
U0702206	0.8	33.30 ± 0.14	0.001 ± 0.001	12.06 ± 0.49	963.0	89.3	29.74 ± 0.19	87.65 ± 0.65
U0702209	0.8	29.98 ± 0.69	0.035 ± 0.284	1.20 ± 12.51	16.9	98.8	29.63 ± 3.76	87.33 ± 10.82
U0702211	0.8	32.18 ± 0.13	0.005 ± 0.043	14.67 ± 1.36	114.5	86.5	27.85 ± 0.42	82.19 ± 1.25
MK-52 - rims	**MK-52-1, d17**	**J=0.001674**						
U0702202	0.8	32.75 ± 0.10	0.003 ± 0.019	11.20 ± 0.53	185.9	89.9	29.45 ± 0.18	86.81 ± 0.62
U0702205	0.8	34.34 ± 0.11	0.000 ± 0.001	21.31 ± 1.31	> 1000	81.7	28.05 ± 0.40	82.77 ± 1.20
U0702207	0.8	31.76 ± 0.13	0.047 ± 0.048	15.27 ± 2.05	12.5	85.8	27.26 ± 0.62	80.49 ± 1.81
U0702208	0.8	29.71 ± 0.25	0.017 ± 0.100	6.36 ± 4.18	34.9	93.7	27.83 ± 1.26	82.15 ± 3.64
U0702212	0.8	34.17 ± 0.22	0.360 ± 0.047	25.83 ± 2.39	1.6	77.8	26.59 ± 0.73	78.57 ± 2.13
MK-99	**MK-99-DS, d17**	**J=0.001674**						
U0703101	0.8	36.29 ± 0.25	0.000 ± 0.000	16.04 ± 0.93	> 1000	86.9	31.55 ± 0.35	92.85 ± 1.07
U0703102	0.8	35.97 ± 0.30	0.000 ± 0.000	22.20 ± 1.53	> 1000	81.8	29.41 ± 0.51	86.71 ± 1.52
U0703103	0.8	30.90 ± 0.14	0.000 ± 0.000	10.74 ± 0.29	> 1000	89.7	27.73 ± 0.15	81.86 ± 0.55
U0703106	0.8	34.54 ± 0.16	0.000 ± 0.000	14.70 ± 0.68	> 1000	87.4	30.20 ± 0.25	88.97 ± 0.79
U0703107	0.8	33.71 ± 0.13	0.000 ± 0.000	10.78 ± 0.56	> 1000	90.5	30.52 ± 0.21	89.90 ± 0.69
U0703108	0.8	32.21 ± 0.22	0.000 ± 0.000	13.00 ± 2.00	> 1000	88.1	28.37 ± 0.62	83.71 ± 1.82
U0703109	0.8	37.83 ± 0.65	0.000 ± 0.000	13.14 ± 6.66	> 1000	89.7	33.95 ± 2.05	99.71 ± 5.88
U0703110	0.8	47.17 ± 1.60	0.000 ± 0.000	57.17 ± 11.78	> 1000	64.2	30.28 ± 3.79	89.21 ± 10.90
MK-99	**MK-99-f, d17**	**J=0.001687**						
U0702301	0.8	32.96 ± 0.15	0.355 ± 0.026	17.79 ± 0.86	1.7	84.2	27.76 ± 0.28	82.58 ± 0.88
U0702302	0.8	37.62 ± 0.53	0.564 ± 0.089	34.23 ± 2.46	1.0	73.3	27.59 ± 0.81	82.08 ± 2.39
U0702303	0.8	33.57 ± 0.11	0.000 ± 0.000	13.72 ± 1.26	> 1000	87.9	29.52 ± 0.39	87.67 ± 1.17
U0702304	0.8	33.11 ± 0.16	0.000 ± 0.000	14.23 ± 1.17	> 1000	87.3	28.90 ± 0.37	85.89 ± 1.13
U0702305	0.8	36.11 ± 0.49	0.000 ± 0.000	23.93 ± 4.57	> 1000	80.4	29.04 ± 1.41	86.27 ± 4.10
U0702306	0.8	33.96 ± 0.27	0.000 ± 0.000	13.31 ± 0.88	> 1000	88.4	30.03 ± 0.36	89.16 ± 1.09
U0702307	0.8	41.28 ± 0.48	0.000 ± 0.000	12.29 ± 8.20	0.0	92.9	37.65 ± 2.46	111.09 ± 7.06
U0702308	0.8	32.34 ± 0.09	0.000 ± 0.000	14.17 ± 1.16	> 1000	87.1	28.15 ± 0.35	83.70 ± 1.07
U0702309	0.8	33.79 ± 0.10	0.000 ± 0.000	15.17 ± 0.52	> 1000	86.7	29.31 ± 0.17	87.07 ± 0.61
U0702310	0.8	37.09 ± 0.12	0.000 ± 0.000	22.95 ± 0.55	> 1000	81.7	30.31 ± 0.19	89.95 ± 0.66
U0702311	0.8	33.88 ± 0.17	0.000 ± 0.000	13.97 ± 0.46	> 1000	87.8	29.75 ± 0.21	88.34 ± 0.69
TSZR	**TSZR**	**J=0.001764**						
U0900304	0.7	31.04 ± 0.27	0.008 ± 0.606	34.95 ± 1.41	77.3	66.7	20.71 ± 0.47	64.73 ± 1.48
U0900305	0.7	43.06 ± 0.20	1.415 ± 0.771	74.53 ± 2.01	0.4	49.3	21.25 ± 0.61	66.39 ± 1.90
U0900307	0.7	46.77 ± 1.00	5.120 ± 4.312	90.11 ± 9.27	0.1	44.5	20.91 ± 2.88	65.35 ± 8.83
U0900308	0.7	34.67 ± 0.25	1.247 ± 0.789	43.63 ± 1.65	0.5	63.3	21.96 ± 0.53	68.57 ± 1.65
U0900311	0.7	38.99 ± 0.42	0.020 ± 2.254	58.08 ± 4.02	29.5	56.0	21.83 ± 1.24	68.18 ± 3.82
TSZR	**TSZR**	**J=0.001764**						
U0900301	0.7	85.69 ± 0.78	0.026 ± 2.204	164.96 ± 6.22	22.2	43.1	36.95 ± 1.89	113.92 ± 5.66
U0900302	0.7	104.44 ± 1.07	0.030 ± 2.215	257.66 ± 6.24	19.7	27.1	28.31 ± 1.80	87.91 ± 5.48
U0900303	0.7	40.65 ± 0.48	0.025 ± 2.319	32.93 ± 4.59	23.2	76.1	30.92 ± 1.46	95.82 ± 4.43
U0900306	0.7	43.98 ± 0.78	4.165 ± 4.442	38.33 ± 11.60	0.1	75.5	33.33 ± 3.56	103.08 ± 10.71
U0900309	0.7	40.91 ± 0.38	0.710 ± 2.531	53.07 ± 4.32	0.8	61.9	25.34 ± 1.34	78.90 ± 4.10
U0900310	0.7	64.08 ± 0.79	1.052 ± 2.303	70.40 ± 3.59	0.6	67.8	43.46 ± 1.22	133.27 ± 3.64